Capillary-fed, thin film evaporation devices

Geoffrey Vaartstra, Lenan Zhang, Zhengmao Lu, et al.

View Online   Export Citation   CrossMark

ARTICLES YOU MAY BE INTERESTED IN

Capillary-fed, thin film evaporation devices

Geoffrey Vaartstra,[1] (ID) Lenan Zhang,[1] (ID) Zhengmao Lu,[2] (ID) Carlos D. Díaz-Marín,[1] (ID) Jeffrey C. Grossman,[2] (ID) and Evelyn N. Wang[1,a] (ID)

AFFILIATIONS

[1]Department of Mechanical Engineering, Massachusetts Institute of Technology, Cambridge, Massachusetts 02139, USA
[2]Department of Materials Science and Engineering, Massachusetts Institute of Technology, Cambridge, Massachusetts 02139, USA

[a]Author to whom correspondence should be addressed: enwang@mit.edu

ABSTRACT

Evaporation plays a critical role in a range of technologies that power and sustain our society. Wicks are widely used as passive, capillary-fed evaporators, attracting much interest since these devices are highly efficient, compact, and thermally stable. While wick-based evaporators can be further improved with advanced materials and fabrication techniques, modeling of heat and mass transport at the device level is vital for guiding these innovations. In this perspective, we present the design and optimization of capillary-fed, thin film evaporation devices through a heat and mass transfer lens. This modeling framework can guide future research into materials innovations, fabrication of novel architectures, and systems design/optimization for next generation, high-performance wick-based evaporators. Furthermore, we describe specific challenges and opportunities for the fundamental understanding of evaporation physics. Finally, we apply our modeling framework to the analysis of two important applications—solar vapor generation and electronics cooling devices.

NOMENCLATURE

A	evaporator area [m^2]
c_p	specific heat at constant pressure [J/kg K]
D	evaporator diameter [m]
D_v	diffusivity of vapor in gas [m^2/s]
$d_{particle}$	characteristic particle size [m]
d_{wick}	characteristic pore size [m]
Ga	gallium
Gr	Grashof number
g	acceleration due to gravity [m/s^2]
H	elevation [m]
h_a	convective heat transfer coefficient to ambient [W/m^2 K]
HTC	heat transfer coefficient [W/m^2 K]
h_{lv}	enthalpy of vaporization [J/kg]
j	mass flux [kg/m^2 s]
j_{dryout}	dryout evaporative mass flux [kg/m^2 s]
k	thermal conductivity [W/mK]
L	characteristic length [m]
L_l	length of effective conduction path from the solid to the liquid-vapor interface [m]
M	figure of merit
$\dot{m}$	evaporation rate [kg/s]

N	nitrogen
$\boldsymbol{n}$	unit normal vector
O	oxygen
P	modified pressure [Pa]
Pe	Péclet number
p	pressure [Pa]
Q	heat transfer rate [W]
q''	heat flux [W/m^2]
q''_{dryout}	dryout evaporative heat flux [W/m^2]
q''_{solar}	incident solar flux [W/m^2]
R	thermal resistance [K/W]
R_g	specific gas constant [J/kg K]
Re	Reynolds number
S	shape factor [m]
T	temperature [K]
t	wick thickness [m]
t_{gap}	air gap thickness [m]
$\boldsymbol{u}$	flow velocity vector [m/s]
u_b	bulk average flow speed [m/s]
$\boldsymbol{u}_m$	mass averaged mixture flow velocity [m/s]
v	specific volume [m^3/kg]
x,y	coordinates in the plane of the wick [m]
z	coordinate normal to the wick plane [m]

Greek symbols

α	solar absorptance
γ	surface tension [N/m]
Δp	capillary pressure [Pa]
Δp_{max}	maximum sustainable capillary pressure [Pa]
$\Delta\rho$	mixture density difference [kg/m^3]
δ	diffusive boundary layer thickness [m]
ε	infrared emissivity
ζ	relative humidity
η	solar-vapor efficiency
θ_e	equilibrium contact angle
θ_{rec}	receding contact angle
K	effective permeability [m^2]
K'	intrinsic permeability [m^2]
κ	mean curvature of the liquid-vapor interface
μ	dynamic viscosity [Pa s]
ν	kinematic viscosity [m^2/s]
ρ	density [kg/m^3]
σ	mass accommodation coefficient
σ_c	condensation coefficient
σ_e	evaporation coefficient
σ_{SB}	Stefan-Boltzmann constant [W/m^2 K^4]
ϕ	porosity
ω	vapor mass fraction

Subscripts

c	condenser
cap	capillary
$cond$	conduction
$conv$	convection
$evap$	evaporation
HK	Hertz-Knudsen
int	liquid-vapor interface
l	liquid
rad	radiation
res	reservoir
S	Schrage
s	solid
sat	saturation
v	vapor
∞	far field

I. INTRODUCTION

Evaporation is an essential mechanism in technologies that provide power,[1] fresh drinking water,[2,3] and cooling for systems ranging from electronics[4] to buildings.[5] The high impact of evaporator performance on these important systems has motivated recent innovation of evaporator materials and configurations,[6,7] along with key advances in our fundamental understanding of liquid–vapor phase change.[8–11] There is still potential to improve system efficiencies by enhancing evaporator thermal performance and reducing the power required to pump liquid to the evaporator. One major thrust of the evaporation community is to advance thin film evaporation (pure evaporation in the absence of boiling) technologies, which are often advantageous due to their stable nature compared to the chaotic boiling process. The use of wicks to achieve capillary-fed, thin film evaporation has attracted much interest because these structures can passively supply liquid, often entirely eliminating the need for a mechanical pump to deliver the working fluid to the evaporator. This advantage reduces system power consumption and is vital for off-grid applications where electricity is scarce or unavailable. Additionally, the presence of a solid wicking structure in the liquid film offers the ability to tune the thermal performance of the evaporator.

Interest in wick-based evaporators has driven efforts to tailor performance via enhancement of intrinsic material properties and wick structures.[12–14] The two key functions of a wick that researchers desire to simultaneously optimize are its ability to supply liquid by capillary pumping and its role in facilitating thermal transport.[4,15,16] Capillary pumping performance can be enhanced by improving the intrinsic wettability of the wick material and designing the structure to minimize viscous dissipation of fluid flow while maximizing the sustainable Laplace pressure. Thermal transport in the wick is influenced by the intrinsic thermal conductivity of the material and the geometry of the porous structure. In certain applications, the wick also acts as a solar absorber,[7,17,18] in which case the radiative absorptance of the wick is an important aspect of the overall thermal transport. Since both capillary pumping and thermal transport performance are connected to the wick's material and structural properties, wick design is often complicated by trade-offs that arise. Although wick performance is often a critical piece of the overall system performance, the working fluid, operating conditions, and system design must also be considered in device-level optimization.

Here, we provide a comprehensive analysis of the physics of heat and mass transport in capillary-fed, thin film evaporation systems and discuss how this knowledge can be applied to developing materials, wick architectures, and system designs. Accurate physical modeling is essential for guiding efficient materials innovation in this field as it allows researchers to understand which novel material properties enhance system performance and to what extent. As shown in Fig. 1, the applications that utilize thin film evaporation differ by many orders of magnitude in size and operating heat flux; consequently, distinct approaches are needed to guide materials and fabrication innovations that push the limits of performance. For instance, the capillary pumping capability of a wick decreases drastically with increasing evaporator size, which is why the use of wicks has largely been focused on systems with smaller evaporators, such as solar vapor generation[17,19–21] and electronics cooling.[4,22] Furthermore, the governing physics of transport from the liquid–vapor interface to the far field are vastly different depending on whether the evaporator is in an air or pure vapor ambient. Our comprehensive heat and mass transport analysis serves as a tool to navigate the modeling of fluidic and thermal pathways under the specific conditions presented by the far field ambient. Additionally, we discuss the challenges and opportunities for advancing our fundamental understanding of liquid–vapor phase change, which will be critical for accurate modeling of high-performance evaporators. Finally, we demonstrate how this modeling framework can be used to guide the design and optimization of capillary-fed, thin film evaporation devices by analyzing its implications for two applications: solar vapor generation and electronics cooling.
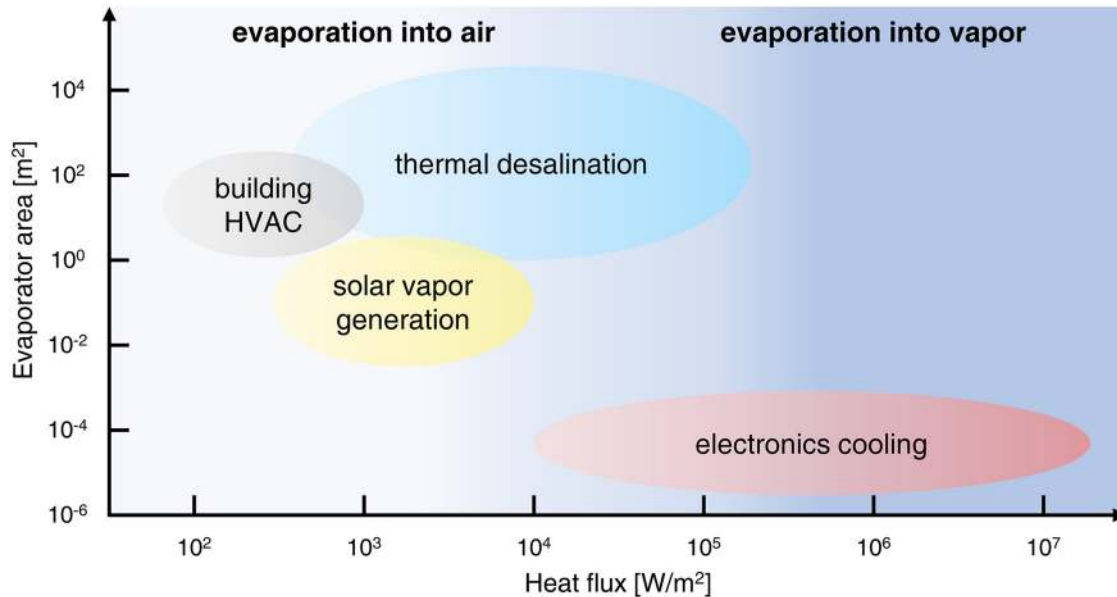
FIG. 1. Operating regimes of processes that use thin film evaporation. Air ambient systems are restricted to lower evaporative heat fluxes than pure vapor systems since the presence of air poses diffusive resistance to mass transport. Capillary-fed devices are typically used for smaller evaporators such as those used in solar vapor generation and electronics cooling due to the size dependence of the capillary pumping limit.

II. LIQUID TRANSPORT

A. Capillary-driven flow

Wicks are porous structures that imbibe liquid on the principle of energy minimization. Imbibition occurs when the solid–vapor specific surface energy (γ_{sv}) is greater than the solid–liquid specific surface energy (γ_{sl}). For a given solid–fluid pair, this criterion is met when the equilibrium contact angle (θ_e) is less than 90°.[23] The driving force for imbibition is characterized by the Young–Laplace equation,

$$\Delta p = p_{l,int} - p_v = 2\gamma_{lv}\kappa, \qquad (1)$$

where Δp is the local capillary pressure, $p_{l,int}$ is the local liquid pressure at the liquid–vapor interface, p_v is the pressure of the vapor phase, γ_{lv} is the liquid–vapor surface tension, and κ is the local mean curvature of the liquid surface.

For passively supplied thin film evaporation, a wick is placed in contact with a stationary liquid reservoir as depicted in Fig. 2(a). In steady state operation, a heat flow (Q) enters the wick and is dissipated to the environment via evaporation, convection, and radiation [Fig. 2(b), "Q_{evap}," "Q_{conv}," and "Q_{rad}," respectively]. Frequently, evaporation is the dominant mode of heat transfer out of the wick, especially in systems where the ambient is pure vapor. Regardless of the ambient conditions, the evaporative heat flux component (Q_{evap}) requires a steady flow of liquid from the reservoir to replenish the evaporating working fluid. This flow of liquid in the wick can be described by

Brinkman's equations,[24]

$$\nabla P = -\frac{\mu_l}{K'}\boldsymbol{u} + \mu_l\nabla^2\boldsymbol{u}, \qquad (2)$$
$$\nabla \cdot \boldsymbol{u} = 0,$$

where $P = p_l + \rho_l g H$ (ρ_l is the liquid density, g is the acceleration due to gravity, and H is the elevation), μ_l is the dynamic viscosity of the liquid, $\boldsymbol{u}$ is the liquid flow velocity vector (vector quantities are henceforth denoted with boldfaced symbols), and K' is the intrinsic permeability of the wick. The mass transferred to the vapor phase via evaporation is accounted for by applying the boundary condition $\rho_l\boldsymbol{u} \cdot \boldsymbol{n} = j_v$ at the liquid–vapor interface, where $\boldsymbol{n}$ is the unit normal vector to the interface pointing into the vapor and j_v is the local evaporative mass flux. Here, we neglect the inertial terms under the assumption that the Reynolds number $\mathrm{Re}_{d_{wick}} = \rho_l u_b d_{wick}/\mu_l \ll 1$, where u_b is the bulk average flow speed and d_{wick} is the characteristic length scale of pores in the wick. K' is generally a second order tensor but is typically denoted as a constant for isotropic and spatially uniform wicks. Alternatively, the momentum conservation statement of Eq. (2) is often expressed using Darcy's law,[25]

$$\nabla P = -\frac{\mu_l}{K}\boldsymbol{u}, \qquad (3)$$

where K is the effective permeability of the wick. This effective permeability accounts for the effects of viscous dissipation within the wick's structure and from its boundaries, whereas the intrinsic permeability only includes the former. Considering a
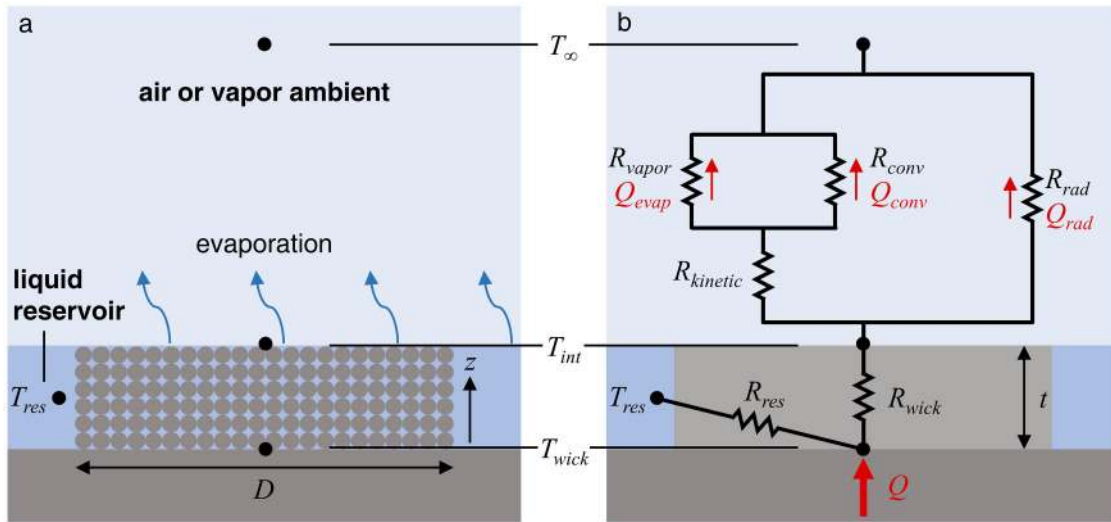
FIG. 2. (a) General schematic of a porous wick evaporator in an air or vapor ambient. A wick adjacent to a stationary liquid reservoir is depicted, but depending on the application, the reservoir may originate at a condenser (as in the case of heat pipes and vapor chambers) or the wick may float on the reservoir. (b) Resistance network representing the thermal paths connecting the wick, reservoir, and ambient. In an air ambient, evaporative heat and mass transport is limited by high resistances to vapor transport (R_{vapor}) and convection (R_{conv}), whereas R_{vapor} is relatively small in a pure vapor ambient, causing resistance in the Knudsen layer ($R_{kinetic}$) to govern the evaporation rate.

common scenario where the wick is attached to a substrate with the liquid reservoir adjacent (as depicted in Fig. 2), K can be determined from Eq. (2) by integrating in the direction normal to the wick plane (z-direction) and enforcing boundary conditions. For this example configuration, scaling of the terms on the right-hand side of Eq. (2) shows that $K \approx K'$ when $K'/t^2 \ll 1$, where t is the thickness of the wick. If the wick has free surface boundaries at both surfaces normal to z, $K = K'$. A similar analysis can be used to apply Darcy's law to a wick in any arbitrary configuration.

B. Dryout limits

The capillary limit of a wick is defined as the operating point where the viscous pressure drop incurred by flow through the wick balances the maximum capillary pressure that can be supplied. This is referred to as the "dryout flux" because dry spots form in regions of the wick where the maximum capillary pressure is exceeded. From Eqs. (1) and (3), it can be seen that this limit will depend on the geometry of the wick's pores, the overall dimensions and orientation of the wick, and the fluid/material properties. We note that the dryout limits do not depend on the ambient vapor conditions (excluding temperature dependence of fluid/material properties), i.e., the dryout limits of a given wick are the same whether operated in air or saturated vapor.

To demonstrate the effects of wick and fluid properties on the performance, we consider a simple case: a disk-shaped, monoporous wick (having one characteristic pore size) of diameter D and thickness t attached to a substrate and surrounded by an adjacent reservoir (as depicted in Fig. 2), pores of size d_{wick}, and negligible effects of gravity. Substituting these parameters into (1) and (3), the

area normalized capillary limited mass flux (kg/m^2 s) and evaporative heat flux (W/m^2) for this system are

$$j_{dryout} = 64 \frac{\gamma_{lv} \rho_l}{\mu_l} \frac{tK}{D^2} \frac{\cos(\theta_{rec})}{d_{wick}},$$

$$q''_{dryout} = 64 h_{lv} \frac{\gamma_{lv} \rho_l}{\mu_l} \frac{tK}{D^2} \frac{\cos(\theta_{rec})}{d_{wick}}, \tag{4}$$

respectively, where h_{lv} is the enthalpy of vaporization of the fluid and θ_{rec} is the receding contact angle for the fluid/solid pair. From this simple case, we extract the capillary transport figure of merit $M_{cap} = h_{lv} \gamma_{lv} \rho_l / \mu_l$,[26] which is used to evaluate the suitability of working fluids at given operating temperatures (see Fig. 3). Equation (4) shows that liquid transport can be enhanced by choosing a fluid with a large M_{cap}, designing a wick that is highly permeable and wetting, and optimizing the dimensions of the wick. In Sec. IV C, we provide further discussion of these design aspects and the trade-offs between wicking and thermal performance.

III. THERMAL TRANSPORT

In typical thin film evaporation devices, heat originates in the solid part of the evaporator by generation (e.g., Joule heating), absorption of radiation, or thermal contact with another body. This heat is conducted through the solid/liquid matrix of the wick, transported to the liquid vapor interface, and is dissipated to the environment by a combination of evaporation, convection, and radiation [Fig. 2(b)]. In thermal management systems, it is common to quantify the heat transfer efficiency using the heat transfer coefficient

(HTC) between the wick and the far field, calculated as

$$\text{HTC} = \frac{q''}{(T_{wick} - T_\infty)}, \tag{5}$$

where q'' is the steady state heat flux dissipated by the wick, T_{wick} is the temperature at the interface between the wick and the heat source, and T_∞ is the temperature of the far field ambient.

Analyzing the paths for dissipation of the heat input to the wick (Q), the thermal resistance R_{res} lumps the conduction and convection resistance from the wick to the liquid reservoir. Depending on the orientation of the wick, R_{res} may be large enough to ignore heat transfer to the reservoir. On the other hand, significant care must be taken to minimize heat losses to the reservoir in applications like solar vapor generation. The solid/liquid matrix of the wick is itself a complicated network for heat transfer from T_{wick} to T_{int} (the liquid–vapor interface temperature), which can be lumped into R_{wick}. Heat transfer from the liquid–vapor interface to the far field strongly depends on the ambient conditions. In air ambient systems, the thermal resistances associated with vapor transport (R_{vapor}) and convection of the background gas (R_{conv}) are dominant over the kinetic resistance ($R_{kinetic}$) due to the large diffusive resistance presented by non-condensable gases.[27] Depending on the system configuration, radiative heat transfer between the wick and the ambient (R_{rad}) can be significant, which is often the case in evaporation from open systems. For systems operating in pure vapor, the diffusive resistance is removed, greatly reducing R_{vapor} such that evaporation is governed by kinetics across the non-equilibrium Knudsen layer,[28,29] quantified by $R_{kinetic}$. In the proceeding sections, we discuss modeling heat transfer in the wick (R_{wick}) and elucidate the distinction between the governing physics for evaporation into air (limited by R_{vapor}) and pure vapor (limited by $R_{kinetic}$).

A. Wick

Due to the typical length scales of wicking structures, R_{wick} is usually dominated by conduction in the solid/liquid matrix. Neglecting advection in the liquid can be justified by evaluating the Péclet number of liquid flow toward the evaporating interface,

$$\text{Pe}_t = \frac{j_v c_p t}{k_l}, \tag{6}$$

where c_p and k_l are the specific heat at constant pressure and thermal conductivity of the liquid, respectively. If $\text{Pe}_t \ll 1$, conduction is the dominant mode of heat transport through the liquid. Thermal Marangoni convection is commonly ignored and was shown to be negligible for typical electronics cooling operating conditions.[30] Since conduction is prevalent, R_{wick} is usually expressed in terms of the wick's effective thermal conductivity (k_{wick}) as

$$R_{wick} = \frac{t}{k_{wick} A}, \tag{7}$$

where A is the area of the evaporator.

The effective thermal conductivity of the wick is dependent on the working fluid, operating conditions, and the material and architecture of the wick. The simplest models for k_{wick} consider the solid and liquid as purely parallel conduction paths,

$$k_{wick} = k_s(1 - \phi) + k_l \phi, \tag{8}$$

or in series,

$$k_{wick} = \frac{k_s k_l}{k_s \phi + k_l(1 - \phi)}, \tag{9}$$

where k_s is the thermal conductivity of the solid and ϕ is the porosity of the wick. The parallel and series models provide upper and lower bounds, respectively, for the effective thermal conductivity. While these models offer some intuition, they do not account for the thermal resistances of constriction, spreading, and tortuosity that are intrinsic to porous media. The Maxwell model for the thermal conductivity of uniform spheres gives

$$k_{wick} = k_s \frac{2 + k_l/k_s - 2\phi(1 - k_l/k_s)}{2 + k_l/k_s + \phi(1 - k_l/k_s)}. \tag{10}$$

This model is often used for sintered particle wicks as a more conservative estimate than parallel conduction, although it still overestimates reported experimental measurements.[31] A comparison of many analytical and empirical models to experimental results for the thermal conductivity of sintered particle wicks was presented by Peterson and Fletcher.[31]

Even highly ordered, non-tortuous wicks like micropillar arrays[32] do not exhibit simple parallel/series behavior when used for thin film evaporation because heat must ultimately be spread from the highly conductive solid into the liquid to enable evaporation. This is often referred to as the "thin film" resistance.[14,32,33] In cases where the thin film resistance contributes significantly to R_{wick}, k_{wick} is sensitive to the wick thickness. Approximate analytical models accounting for constriction, tortuosity, and thin film resistance in specific, highly ordered structures have been developed,[32,34,35] but numerical methods are often necessary to fully capture the complexities of 3D heat flow in wick structures.[15,30,34] From a qualitative point of view, the large relative resistance of the thin film arises from the orders of magnitude difference between k_l and k_s (for example, $k_l/k_s \sim 10^{-3}$ for water and copper at 20 °C). Thus, even if the effective conduction path between the solid–liquid and liquid–vapor interfaces (L_l) is much shorter than the conduction path through the solid, the thin film resistance could be significant. As such, pushing the limits of R_{wick} requires attention to k_s, k_l, t, and L_l. As seen in Eq. (4), decreasing t to reduce R_{wick} comes at the cost of simultaneously reducing the dryout heat flux.[15] Another conflict between designing for thermal resistance and dryout heat flux comes into play due to the fact that L_l cannot be decreased independently from d_{wick} in monoporous wicks. We discuss these trade-offs as they relate to electronics cooling devices in Sec. IV C.

B. Air ambient

In an air ambient, the flow of vapor away from an evaporator is hindered by frictional resistance from air molecules. This resistance is much stronger than the kinetic resistance under typical air ambient conditions, as evidenced by the good fit of purely continuum diffusive/convective models to experimental data.[27,36–38] Thus, transport in the Knudsen layer can be neglected for evaporators operating in an air or non-condensable gas ambient. The most general approach to determine the evaporation rate is to first solve the coupled mass, momentum, and energy conservation equations with appropriate boundary conditions to determine the mass average mixture flow velocity (u_m). Then, the evaporative flux can be determined from the advection–diffusion equation,

$$j_v = \rho\omega u_m - \rho D_v \nabla\omega, \tag{11}$$

where j_v is the vapor mass flux vector, ρ is the mixture density, ω is the vapor mass fraction, and D_v is the diffusivity of vapor in the gas (or mixture of gases). The evaporative mass flux is related to the evaporative heat flux by $q''_{evap} = j_v h_{lv}$, so the equivalent thermal resistance is

$$R_{vapor} = \frac{T_{int} - T_\infty}{j_v h_{lv} A}. \tag{12}$$

Determination of the flow velocity is often a non-trivial task, but we will only consider commonly encountered limits of Eq. (11) as the conservation equations and various methods to solve them are discussed in the literature and heat/mass transfer textbooks.[26,39] R_{conv} can also be determined using classical heat and mass transfer solutions.

It is common to approach device-level modeling by considering limits in which certain terms of the conservation equations can be neglected, or by using correlations provided by rigorous analytical, numerical, or experimental evaluation of the conservation equations. In the limit of purely diffusive transport in a binary system, the evaporative mass flux is modeled by Fick's law,[26]

$$j_{Fick} = -\rho D_v \nabla\omega. \tag{13}$$

Fick's law is widely used for evaporation into air, yet caution must be taken in noting that it is valid under the conditions that (a) the diffusing species is dilute and (b) advection can be neglected. When the evaporative flux is sufficiently large, advection of the vapor (known as Stefan flow) can no longer be ignored. The balance between advective and diffusive transport is characterized by the Péclet number,

$$Pe_\delta = \frac{u_{m,int}\delta}{D_v}, \tag{14}$$

where $u_{m,int}$ is the velocity of the mixture near the interface and δ is an effective boundary layer thickness that depends only on system geometry and boundary conditions.[27] δ relates to the shape factor S of a system by $\delta = A/S$; care should be taken in

recognizing that S (and therefore δ) may scale up with the size of the evaporator.[26] Values of S are tabulated for many simple configurations[26] or can be determined experimentally for a specific geometry.

For conditions with a high Pe_δ or vapor concentration such that Fick's law becomes invalid, the advection–diffusion equation (also known as the Maxwell–Stefan equation) should be applied.[40] Simplifying for binary transport, zero net flow of the ambient gas, and no external pressure gradient, the Maxwell–Stefan equation reduces to

$$j_{Stefan} = -\rho D_v \nabla \ln\left(\frac{1}{1-\omega}\right), \tag{15}$$

where j_{Stefan} is the vapor mass flux, including both advection and diffusion. For 1D flow in terms of the effective boundary layer thickness, temperature of the interface, and far field vapor mass fraction (ω_∞),

$$j_{Stefan} = -\frac{\rho D_v}{\delta} \ln\left(\frac{1-\omega_{sat}(T_{int})}{1-\omega_\infty}\right), \tag{16}$$

where $\omega_{sat}(T_{int})$ is the saturated vapor mass fraction at T_{int}. While the forms of Eqs. (15) and (16) are applicable for many evaporators, the general form of the advection–diffusion equation [Eq. (11)] is valid for conditions including flow of the ambient gas and can be generalized for multicomponent mixtures.[40] Lu *et al.* demonstrated that Fick's law underpredicted experimental results for high-flux evaporation into air, whereas the Maxwell–Stefan equation fit their data well for all experimental conditions tested (up to Pe_δ and $\omega_{sat}(T_{int})$ of nearly unity).[27]

The effects of gravity sometimes must be considered in evaporative systems. Buoyancy driven advection (natural convection) is quantified by the Grashof number of the system,

$$Gr = \frac{g\Delta\rho L^3}{\rho v^2}, \tag{17}$$

where $\Delta\rho$ is the difference in mixture density between the interface and far field, L is the characteristic length scale of the system, and v is the kinematic viscosity of the mixture. When $Gr \ll 1$, natural convection can be neglected; otherwise, numerous correlations exist for heat/mass transfer due to natural or externally forced convection in a variety of configurations.[26] When considering the scalability of laboratory-scale systems, it is important to recognize that the size dependence of δ and Gr may cause the transport physics to change significantly with the system scale. Finally, it should be noted that effects such as Stefan flow, natural convection, and external convection may exhibit complicated coupling when more than one is present in a system. For instance, Zhang *et al.* recently analyzed the interplay between Stefan flow and natural convection and provided heat/mass transfer correlations for this mixed mode.[41]

C. Pure vapor ambient

A saturated vapor ambient is preferred for steam turbines,[1] mechanical vapor compression desalination systems,[3] and electronics cooling devices[4] since heat transfer efficiency is enhanced by removing the diffusion resistance presented by non-condensable

gases. In the absence of diffusion resistance, R_{vapor} can be of the same order as $R_{kinetic}$ or even smaller, depending on the device configuration. For devices like heat pipes, where the resistance to vapor flow returning to the condenser may not be negligible, R_{vapor} should be considered in series with $R_{kinetic}$ to determine the system performance. We offer a brief discussion of device-level modeling in Sec. IV C. Here, we discuss the underlying physics of kinetically limited heat transfer since this limit is becoming increasingly important as materials, fabrication, and systems design advances diminish R_{wick} and R_{vapor}.

Classic kinetic theory considers that a net evaporation/condensation flux across the liquid–vapor interface perturbs the local thermodynamic equilibrium in the vapor phase, giving rise to the non-equilibrium Knudsen layer adjacent to the interface.[42] Since equilibration is driven by molecular collisions, the Knudsen layer is typically a few mean free paths thick.[29] Various models exist that connect Knudsen layer kinetics to macroscopic external flow variables (e.g., heat flux), the most common of which are the Hertz–Knudsen (HK) and Schrage equations,[28] which express the evaporative heat flux as

$$q''_{HK} = \frac{h_{lv}}{\sqrt{2\pi R_g}} \left(\sigma_e \frac{p_{sat}(T_{l,int})}{\sqrt{T_{l,int}}} - \sigma_c \frac{p_{v,\infty}}{\sqrt{T_{v,\infty}}} \right),$$
$$q''_S = \frac{2}{2 - \sigma_c} \frac{h_{lv}}{\sqrt{2\pi R_g}} \left(\sigma_e \frac{p_{sat}(T_{l,int})}{\sqrt{T_{l,int}}} - \sigma_c \frac{p_{v,\infty}}{\sqrt{T_{v,\infty}}} \right),$$

(18)

where R_g is the specific gas constant, $p_{sat}(T_{l,int})$ is the saturation pressure at $T_{l,int}$, σ_e is the evaporation coefficient, and σ_c is the condensation coefficient. σ_e denotes the fraction of vapor molecules emitted from the liquid compared to the amount predicted
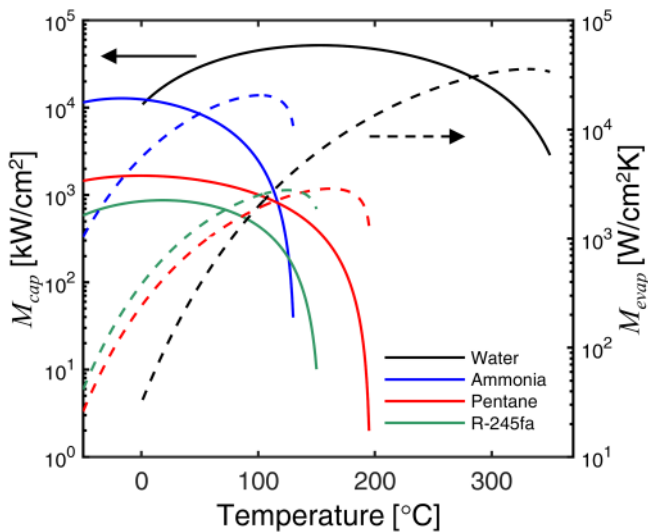

FIG. 3. Merit numbers of select working fluids over a range of operating temperatures. The solid and dashed lines correspond to M_{cap} and M_{evap}, respectively. While water has superior properties for capillary liquid transport, the other fluids shown here are more favorable for efficient evaporative heat transfer between 0 and 97 °C.

by the equilibrium Maxwell–Boltzmann distribution, while σ_c is the probability that a vapor molecule impinging on the interface condenses.[43] At near equilibrium conditions (low Mach number), it is widely agreed that $\sigma_e = \sigma_c = \sigma$,[29,44] referred to here as the mass accommodation coefficient. The Schrage equation is more appropriate for evaporation into a large vapor reservoir as it accounts for the external vapor flow while the HK equation does not, although Ytrehus pointed out that the HK equation is correct for free molecular evaporation/condensation between parallel, planar liquid surfaces.[29] However, it has been acknowledged that neither the HK nor the Schrage equation explicitly conserves momentum and energy.[29,45] We note that the Schrage equation as shown in Eq. (18) is simplified for low Mach number conditions; the full equation provides better accuracy for high-speed flows.[44]

A more rigorous theoretical approach is to consider the governing equation for the evolution of the molecular velocity distribution function across the Knudsen layer, the Boltzmann transport equation (BTE).[46] The complicated nature of the BTE collision term makes analytical solutions not possible for most problems, but a large body of literature exists containing perturbation-theory-based solutions,[42,47] moment solutions,[29,48] numerical solutions to the Boltzmann–Krook–Welander (BKW) model equation,[49–52] and direct simulation Monte Carlo (DSMC) solutions.[46,53–55] We note that numerical BKW and DSMC solutions are regarded as most accurate.[29] Extension to polyatomic gases was analyzed thoroughly by Frezzotti.[56] Recently, Lu et al. demonstrated that the HK and Schrage equations and a polyatomic DSMC solution to the BTE showed reasonable agreement to experimental results for low Mach number evaporation of water into its pure vapor.[57] Other recent molecular dynamics (MD) studies have characterized the validity of the Schrage equations for evaporation of argon in steady state[58] and transient[59] conditions.

While thermal resistance between the wick and the interface (R_{wick}) is predominantly controlled by the wick material and geometry, Eq. (18) shows that the resistance to evaporation is set by the working fluid and operating conditions. Using the Schrage equation, the thermal resistance at the liquid–vapor interface is commonly expressed as[44]

$$R_{kinetic} = \frac{1}{A_{int}} \left(\frac{2 - \sigma}{2\sigma} \right) \left(\frac{T_{v,\infty} v_{lv}}{h_{lv}^2} \right) (2\pi R_g T_{v,\infty})^{1/2} \left(1 - \frac{p_{v,\infty} v_{lv}}{2h_{lv}} \right)^{-1},$$

(19)

where A_{int} is the area of the liquid–vapor interface and v_{lv} is the specific volume difference between phases. We note that Eq. (19) only considers heat transfer due to evaporation, a reasonable assumption for most practical systems. Conduction across the Knudsen layer is typically negligible but has been shown to be an appreciable mode of heat transfer for small systems (~100 nm length scale) where non-condensable gases are present.[60,61]

A kinetically limited heat flux scaling can be expressed by rearranging (18) and assuming a small temperature difference between the liquid and vapor,

$$q''_{kinetic} \sim \frac{h_{lv}}{\sqrt{R_g T_{v,\infty}}} \frac{dp}{dT}\bigg|_{sat} (T_{l,int} - T_{v,\infty}),$$

(20)

where $\frac{dp}{dT}\big|_{sat}$ is the derivative of the equilibrium vapor pressure with respect to temperature along the saturation line. From Eq. (20), we extract an evaporation figure of merit for the fluid, $M_{evap} = \frac{h_{lv}}{\sqrt{R_g T_{v,\infty}}} \frac{dp}{dT}\big|_{sat}$, where $\frac{dp}{dT}\big|_{sat}$ is evaluated at $T_{v,\infty}$. We note that M_{evap} gives a heat flux scaling per unit temperature rise, whereas the evaporation figure of merit proposed by Lu et al.[57] and Hanks et al.[62] relates to heat flux via a dimensionless driving pressure. Both figures of merit are derived from the same physical principle and are equally valid; here, we prefer to provide intuition for thermal resistance directly from M_{evap}. We plot both the capillary and evaporation figures of merit for various fluids in Fig. 3. M_{evap} does not account for mass accommodation, which is widely believed to be a function of temperature[63] and strongly depends on the working fluid. While σ is generally taken to be close to unity for non-polar fluids, various theoretical and experimental works have reported values of σ spanning three orders of magnitude (0.001–1) for water.[43] Determination of the mass accommodation coefficients of pure fluids is still an active area of research,[8,11] but modeling of practical systems is further confounded by the sensitivity of the accommodation coefficient to contaminants.[43] For this reason, σ is often treated as a fitting parameter to be experimentally determined for a given evaporator, working fluid, and range of operating conditions.[32,62]

IV. CHALLENGES AND OPPORTUNITIES IN THIN FILM EVAPORATION

A. Fundamental understanding

As innovative fabrication techniques allow access to evaporation/condensation regimes that approach the fundamental limit of interface resistance dominated transport, a thorough understanding of the liquid–vapor interface is critical. When considering the kinetics of liquid–vapor phase change at near equilibrium conditions, the typical approach is to (a) assume that particles are emitted from the interface into the vapor according to the equilibrium distribution, i.e., a half Maxwellian distribution for the velocity component normal to the interface;[52] (b) assume diffuse reflection[29,52] of vapor molecules that do not accommodate into the liquid phase upon striking the interface; (c) assign a mass accommodation coefficient to describe the probability of exchange between phases; and (d) couple the liquid–vapor interface boundary condition to the external vapor flow. MD has provided evidence that (b) is accurate under various conditions;[60,61,64,65] however, the validity of (a) is unclear as some molecular dynamics studies have predicted a non-Maxwellian distribution for the normal velocity component due to the influence of the liquid's potential well.[66,67] As such, the velocity distribution of molecules emitted from the interface into the vapor as well as the value and fundamental mechanism behind the mass accommodation coefficient are open questions of great interest. Nagayama and Tsuruta[63] proposed a theoretical framework to describe the condensation coefficient using the transition state theory,[68] but MD calculations were used to fit their model due to a lack of physical understanding of the energy barrier proposed by their theory. A statistical rate theory approach was used by Ward and Fang to derive an expression for evaporation flux,[69] but their result requires the determination of thermodynamic conditions precisely at the interface, making it difficult to apply in practice. Bedeaux et al. analyzed the liquid–vapor interface from a non-equilibrium thermodynamics perspective and supported the expression of Nagayama and Tsuruta for the condensation coefficient when an energy barrier exists.[70] Since the origin of this energy barrier is unclear, it remains an open question that requires more in-depth theoretical and experimental investigations. The complex molecular picture at the boundary between phases seems to point to molecular dynamics as a promising pathway to a better understanding of the fundamental properties of the liquid–vapor interface.

While MD studies have continued to improve our theoretical understanding in recent years,[8–10] there have also been advancements in experimental techniques to study the liquid–vapor interface. Experimental determination of the mass accommodation coefficient, for instance, is challenging because (a) temperature must be measured precisely at the interface without disturbing gas kinetics; (b) contaminants cannot be allowed to concentrate at the interface; and (c) it is difficult to design an experiment where transport is highly sensitive to the properties of the liquid–vapor interface. Figure 4(c) demonstrates the significant discrepancy between experimental[11,57,71–74] and MD[9,63] reported values of the mass accommodation coefficient of water and highlights the large uncertainty of experimental measurements. Nonetheless, state-of-the-art fabrication and measurement techniques enable experimental studies that bring us ever closer to precise, reliable measurements of σ. Li et al. fabricated a hybrid nanofluidic channel that allowed accurate measurement of the evaporation rate of water from a few nanopores by visualizing the receding meniscus in a nanochannel [Fig. 4(b)].[74] However, the temperature of the liquid–vapor interface was not monitored, and the nanopore diameter-dependence they had observed was attributed to contaminant buildup. Lu et al. designed a nanoporous membrane evaporator that provided non-invasive temperature sensing at the liquid–vapor interface with continuous flow underneath the membrane to advect away contaminants.[57] Nevertheless, the purpose of that study was to validate the kinetic theory model for the Knudsen layer; the accommodation coefficient was obtained by applying a model fit to the BTE. Although Lu et al. relied on state-of-the-art nanofabrication to create a resistance temperature detector (RTD) adjacent to the liquid–vapor interface,[57] others have used optical techniques like Raman thermometry to measure substrate temperature precisely at the three-phase contact line[75] or directly measure the bulk temperature of water droplets.[72] Lee et al. circumvented the need for location-sensitive temperature sensing by measuring the mass accommodation coefficient using isothermal, forward osmosis-driven flow across a thin vapor gap in a membrane [Fig. 4(a)].[11] While improved sensitivity was achieved, measurement uncertainty was still $\approx 50\%$ and the effect of solutes in their draw solution could not be quantified. The challenges and opportunities in this space lie in further increasing experimental sensitivity to the mass accommodation coefficient while simultaneously meeting the temperature sensing and contaminant mitigation requirements.

B. Solar vapor generation devices

Solar vapor generation, applying direct solar heating to drive evaporation, plays a ubiquitous role in steam generation,[7,17,18]
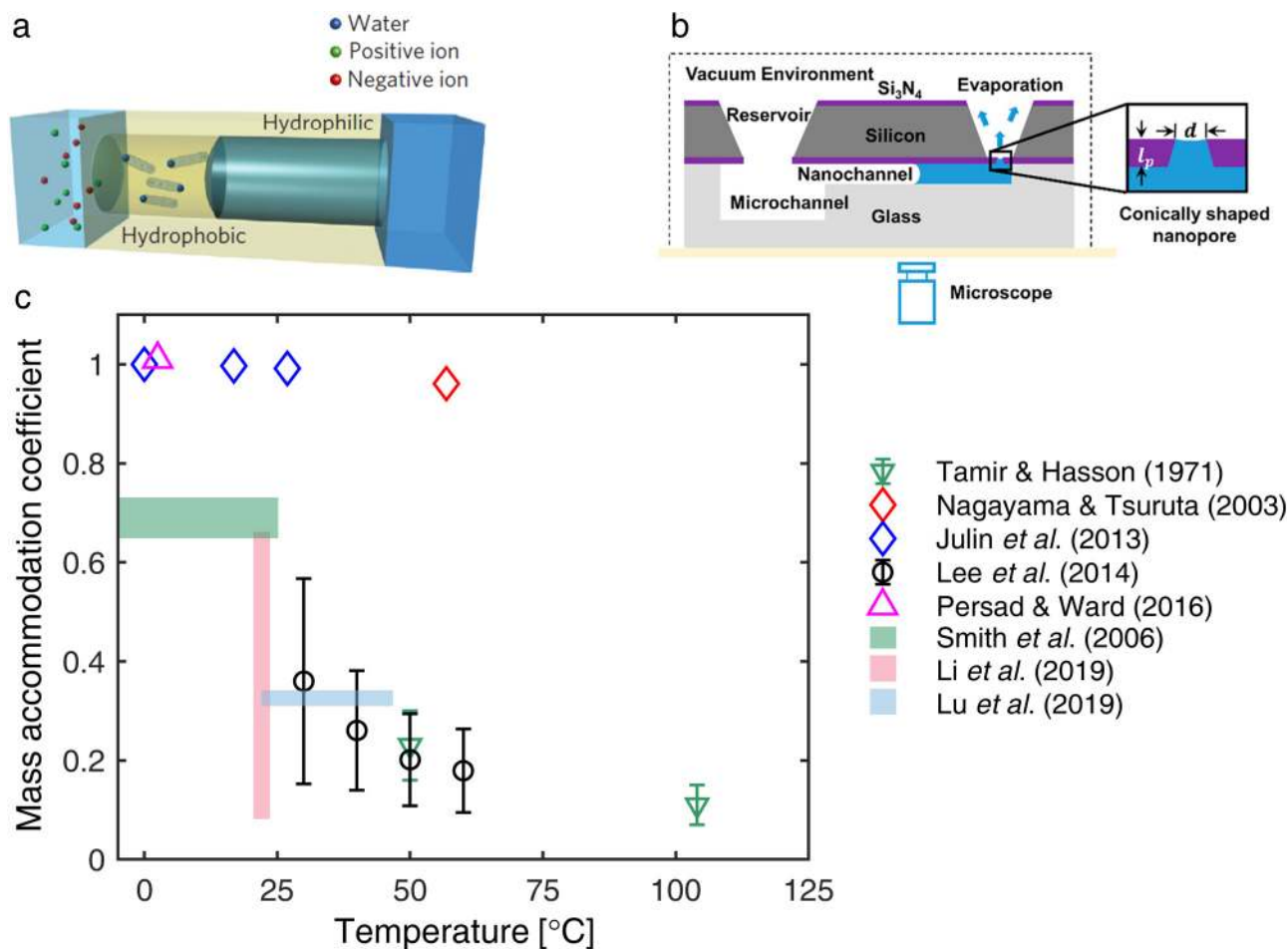
FIG. 4. (a) Depiction of the vapor gap membrane designed by Lee *et al.*[11] to measure σ via forward osmosis-driven transport. Adapted with permission from Lee *et al.*, Nat. Nanotechnol. **9**, 317 (2014). Copyright 2014 Springer Nature. (b) Schematic of the nanofluidic device used by Li *et al.*[74] to measure σ through thermally driven evaporation. Adapted with permission from Li *et al.*, ACS Nano **13**, 3363 (2019). Copyright 2019 American Chemical Society. (c) A selection of reported values of the mass accommodation coefficient of water from the literature. The green (Smith *et al.*[72]) and blue (Lu *et al.*[57]) shaded regions represent a single value of σ (with uncertainty bands) measured over a range of temperature conditions. The red shaded region (Li *et al.*[74]) represents multiple reported values of σ corresponding to different diameter nanopores. The diamond symbols represent MD calculations, which consistently predict $\sigma \approx 1$. The remainder of the data is comprised of experimental measurements that tend to fall well short of unity and have wide uncertainty bands due to the difficulty of achieving high sensitivity.

desalination,[21,76–79] sterilization,[7,80] and wastewater treatment.[81] Recently, solar-driven interfacial evaporation, which localizes the solar-thermal energy at the liquid/air interface through a solar absorbing capillary wick structure, has attracted particular interest due to its passive, high-efficiency, portable, and low-cost nature. Compared with the volumetric heating configuration, interfacial evaporation reduces the required thermal mass and avoids heat loss through the bulk liquid, which therefore improves the overall solar vapor conversion efficiency.[7] In typical solar-driven interfacial evaporation, a floating capillary wick is used as the evaporator (Fig. 5).[7,18] Liquid is driven by capillary pressure due to the micro-to-nanopores of the wick. Additionally, the capillary wick has high absorption to visible light, which enables efficient solar-thermal energy conversion. Owing to the low thermal conductivity of the wick (i.e., high R_{wick}), thermal energy is localized at the interface where evaporation occurs. Compared with the requirement of high solar absorption and low thermal conductivity, wickability plays a relatively insignificant role to the overall performance because non-concentrated solar flux ($\sim$1000 W/m^2) is typically much smaller than the capillary limit of the wick. Although significant achievements have been demonstrated in both material synthesis and device characterization, the fundamental heat and mass transport during solar vapor generation has been left largely unexamined. Therefore, a unified theoretical treatment is required that considers the interplay among the passive liquid feed, coupling of interfacial heat and mass transport, vapor diffusion into the air ambient, and the overall solar-to-thermal energy conversion. The fundamental limit and the general optimization principle need to be well-understood based on quantitative analysis.
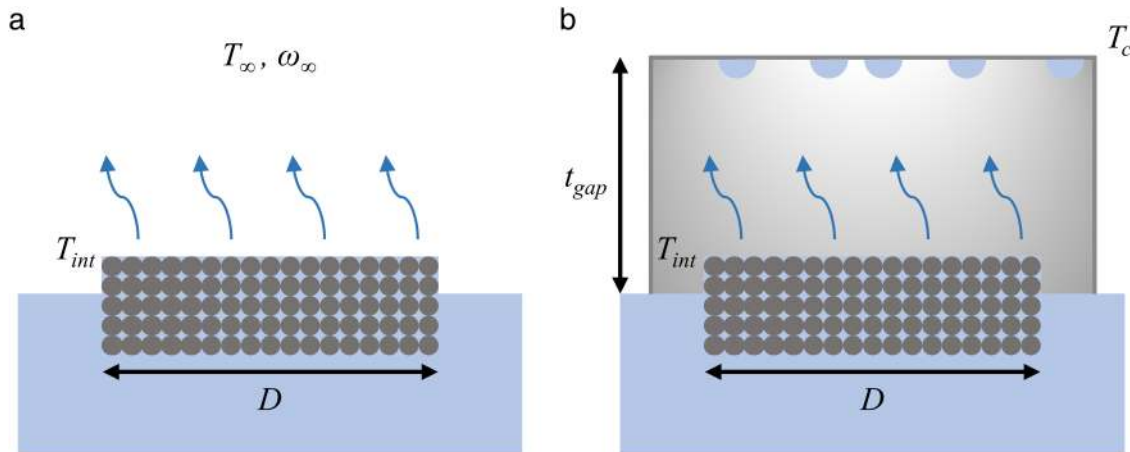
FIG. 5. Schematics of porous wick evaporators operating in (a) open and (b) closed configurations. For an open system, the evaporative flux is highly dependent on the vapor mass fraction at the far field. The mass transport resistance is only a function of the evaporator size (scaling with $1/D$), which is independent of material properties. For a closed system, both the evaporator and condenser are in a saturated state; consequently, the mass transport resistance increases with the air gap thickness t_{gap} but is independent of D.

This general theoretical description of the vapor diffusion can be further used to model and understand the fundamental heat and mass transport in solar vapor generation systems. Considering solar-thermal energy conversion, evaporative heat transfer, radiative and convective heat loss to the air ambient, and conductive heat loss to the bulk liquid, the energy balance of an evaporator in a steady state can be expressed as[17]

$$\dot{m}h_{lv} = A\alpha q''_{solar} - A\varepsilon\sigma_{SB}(T_{int}^4 - T_\infty^4) - Ah_a(T_{int} - T_\infty) - Q_{cond} \tag{21}$$

where $\dot{m} = Aj_v$ is the evaporation rate which can be determined from Eq. (13) or Eq. (16) depending on the operation regime. α is the solar absorptance of evaporator and q''_{solar} is the incident solar flux along the surface normal. ε and σ_{SB} are the infrared emissivity of evaporator and Stefan–Boltzmann constant, respectively. h_a is the convective heat transfer coefficient of the ambient air and Q_{cond} is the conductive heat transfer rate to the bulk liquid. In a quiescent air ambient, h_a arises from natural convection, which typically ranges from 5 to 15 W/m² K. More accurate estimations of h_a can be obtained from the classic correlations of natural convection[26] and corrected using the correlation provided by Zhang *et al.* for high-flux applications.[41] Note that since solar vapor generation is usually performed under a non-concentrated solar flux (~1000 W/m²),[76,79,82,83] the Maxwell–Stefan effect on j_v and h_a is negligible. However, if a high solar concentration (>10–100) is applied, the accuracy of Fick's law should be carefully examined according to the analysis of Sec. III B.

Equation (21) provides the basic framework to understand the coupling of heat and mass transport in various practical systems. Since R_{vapor} plays a dominant role in the air ambient system, heat and mass transport is determined by the interaction between the capillary wick and surrounding environment. Here, we discuss two representative evaporation configurations, i.e., the open and closed

systems (Fig. 5), and analyze several essential mechanisms that have not been commonly considered in the present analysis of solar-driven interfacial evaporation. In practical applications, the open configuration can be seen in the vapor/steam generation systems while the closed configuration is used in solar-driven desalination or wastewater treatment processes. When evaporation occurs in an open system, i.e., vapor diffuses from the evaporator to the far field air ambient [Fig. 5(a)], the solution to Eq. (13) is determined by the shape factor S of the system as

$$\dot{m} = \rho D_v S(\omega_{sat}(T_{int}) - \omega_\infty). \tag{22}$$

The far field vapor mass fraction is related to the far field relative humidity (ζ_∞) by $\omega_\infty = \zeta_\infty\omega_{sat}(T_\infty)$. S is only determined by the geometry of the system. For example, if a disk-shaped evaporator (with diameter D) is placed into a semi-infinitely large environment, S is equal to $2D$. According to Eqs. (21) and (22), the heat and mass transport during solar-driven interfacial evaporation is a nonlinearly coupled problem. To evaluate the performance of the evaporator, the solar vapor efficiency η is defined as

$$\eta = \frac{\dot{m}h_{lv}}{Aq''_{solar}}. \tag{23}$$

Figure 6 shows the evaporation performance of an open system in some representative conditions by solving Eq. (21). The reference data in Fig. 5 indicate the result when $D = 5$ cm, $h_a = 10$ W/m² K, $D_v = 3 \times 10^{-5}$ m²/s, $\alpha = 0.97$, $\varepsilon = 0.03$, and $\zeta_\infty = 0.1$. The effective thermal conductivity of the liquid filled capillary wick is $k_{wick} = 0.05$ W/mK, and the thickness of the evaporator is $t = 2$ cm. To show the contribution of different parameters, the reference data were compared with different conditions by changing the corresponding parameters. Specifically, since the
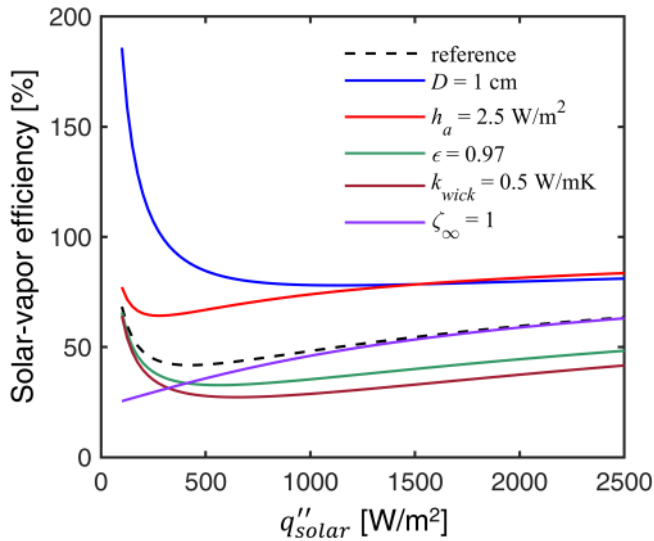
FIG. 6. Simulated solar vapor efficiency of a representative open system modeled by Eq. (21). The vapor efficiency labeled as "reference" indicates the simulation results based on parameters $D = 5$ cm, $h_a = 10$ W/m^2 K, $D_v = 3 \times 10^{-5}$ m^2/s, $\alpha = 0.97$, $\varepsilon = 0.03$, $\zeta_\infty = 0.1$, and $k_{wick} = 0.05$ W/mK. Each of the remaining results is labeled by a specific parameter, indicating only the value of the corresponding parameter that changed while all other parameters are the same as the "reference." For example, the vapor efficiency labeled as "$D = 1$ cm" shows the simulation results based on parameters $D = 1$ cm, $h_a = 10$ W/m^2 K, $D_v = 3 \times 10^{-5}$ m^2/s, $\alpha = 0.97$, $\varepsilon = 0.03$, $\zeta_\infty = 0.1$, and $k_{wick} = 0.05$ W/m K. Code for this model can be found in the supplementary material.

effective boundary layer thickness is $\delta = A/S \sim D$, reducing evaporator size always leads to higher η even if all remaining material properties are held constant. For example, if D decreases from 5 cm to 1 cm, η increases more than 60% under one-Sun illumination (1000 W/m^2) (see the blue curve in Fig. 6). Convection is one of the most dominant sources of heat loss. For example, if h_a could be reduced from 10 W/m^2 K to 2.5 W/m^2 K using a proper convection cover, an ∼60% increase of η can be achieved under one-Sun illumination (bright red curve). A spectrally selective absorber, which has high absorptance to the solar spectra and low emissivity to the infrared spectra, is important to reduce the radiative loss. Otherwise, an ∼35% reduction of η is predicted if a gray-body or blackbody absorber is used (green curve). The effective thermal conductivity of the evaporator is critical to the heat localization. For example, a more than 40% decrease of η is shown under one-Sun illumination if k_{wick} increases from 0.05 W/m K to 0.5 W/m K (dark red curve), which is comparable to the thermal conductivity of liquid water. In general, achieving $\eta > 90\%$ is fundamentally challenging even if a relatively small sized evaporator ($D = 5$ cm), spectrally selective absorber ($\alpha = 0.97$ and $\varepsilon = 0.03$), and superior thermal insulation ($h_a = 2.5$ W/m^2 K and $k_{wick} = 0.05$ W/m K) are applied to the open system.

A key signature of the open configuration is the contribution of dark evaporation. Dark evaporation arises from the concentration difference between the saturated liquid/air interface and the far

field at the ambient temperature, which occurs as long as the far field is not saturated. This dark evaporation effect is also described as "vapor generation by environmental energy" in some studies.[84,85] In most studies, however, the contribution of dark evaporation to vapor generation was eliminated from η by measuring the evaporation rate of the system without solar illumination.[17,18,76,79] For a typical capillary wick with centimeter scale size, dark evaporation dominates the total vapor generation at low solar flux ($q''_{solar} < 250$ W/m^2), while its contribution becomes negligible when q''_{solar} is sufficiently large (>1500 W/m^2). This can be seen in Fig. 6 by comparing the reference curve to the $\zeta_\infty = 1$ condition (purple curve) for which there is no dark evaporation. To obtain an accurate characterization for the solar-to-vapor conversion performance, the dark evaporation rate should be carefully determined especially for the low solar flux regime ($q''_{solar} < 1000$ W/m^2) where ζ_∞ and S should remain the same for both experiments with/ without solar illumination.

On the other hand, when evaporation occurs in a closed system, where an evaporator and a condenser are separated by an air gap [Fig. 5(b)], the heat and mass transport process becomes fundamentally different than in open systems even if the same materials are used for the evaporator. In a one-dimensional case, the mass flow rate across the air gap is given by

$$\dot{m} = \rho D_v A \frac{\omega_{sat}(T_{int}) - \omega_{sat}(T_c)}{t_{gap}}, \quad (24)$$

where T_c is the temperature of the condenser and t_{gap} is the air gap thickness. Comparing Eq. (24) with Eq. (22), there are two significant differences between the closed and open systems. First, vapor transport in a closed system is driven by the concentration gradient between the evaporator and condenser, which is determined by saturation properties at T_{int} and T_c. Second, instead of a constant value [$1/(SD_v)$] at fixed A for the open system, the vapor transport resistance [$t_{gap}/(AD_v)$] can be significantly changed by t_{gap} (from 0 to ∞) for a closed system. Since decreasing t_{gap} results in a simultaneous decrease of the heat conduction and mass transport resistance through the air gap, reducing the mass transport resistance leads to a significant increase of heat loss through conduction in the small air gap thickness regime. Therefore, there is an optimal air gap thickness corresponding to a maximum vapor conversion efficiency, which was discussed recently by Zhang et al.[86]

We show several representative solar vapor generation devices in Figs. 7(a)–7(c) and plot their performance in Fig. 7(d).[13,17,18,21,77,79,82,83,87,88] Multi-stage devices that reuse the latent heat of condensation (solid symbols) exceeded 100% solar vapor efficiency and produced more water than single-stage devices. Although engineering the material properties of the evaporator has been extensively studied to improve vapor production,[13,21,77,89] the fundamental bottleneck of solar vapor generation—especially under a non-concentrated solar flux—is typically not the material-level innovation but the optimization of heat and mass transport at the device level.[78,82,83] For example, Wang et al. showed the opportunities of latent heat recovery through an advanced thermal design for achieving multifold enhancement of water production in the application of passive solar-driven
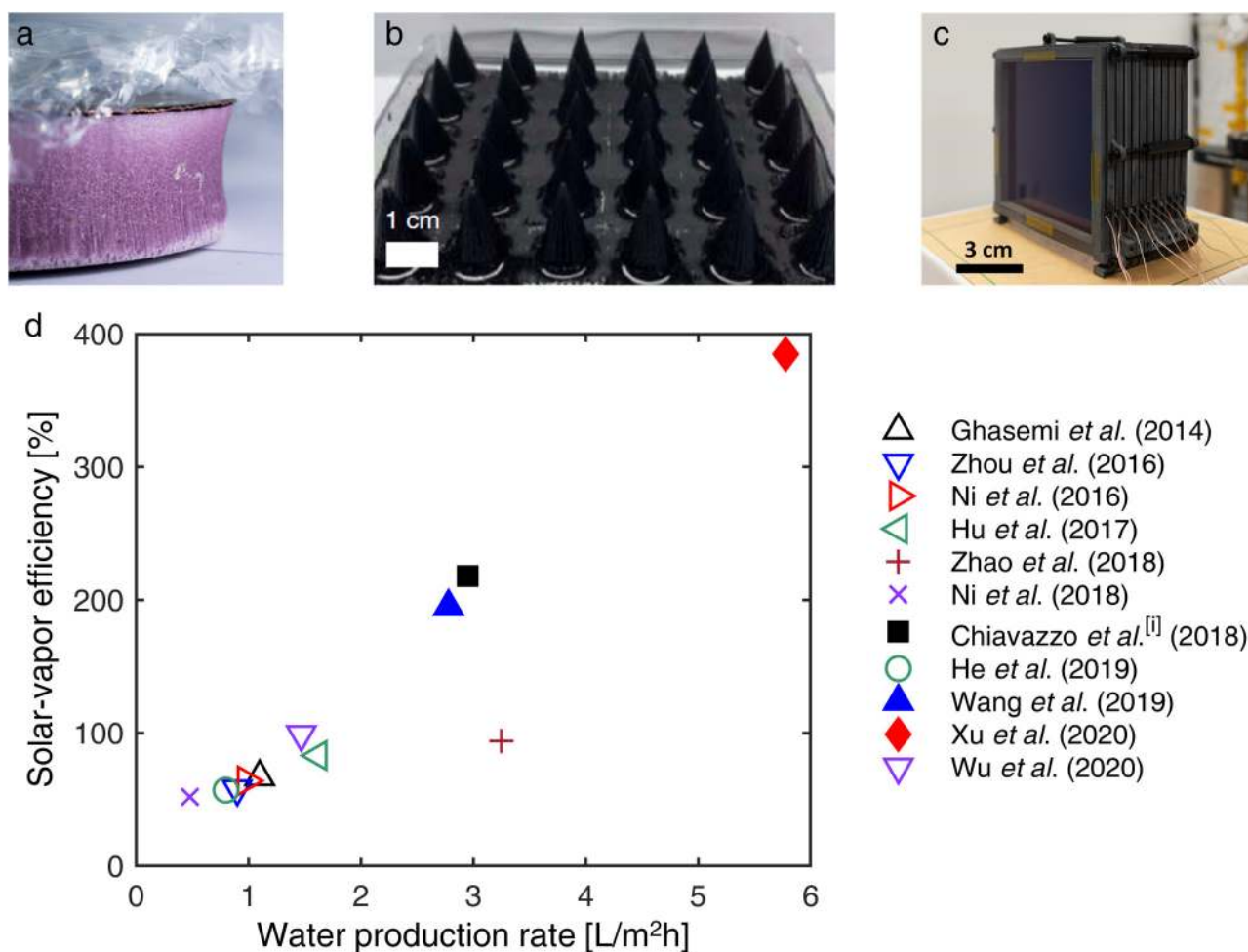
FIG. 7. (a)–(c) Images of solar vapor generation devices/materials reported by (a) Ni et al.[17] [reprinted with permission from Ni et al., Nat. Energy **1**, 16126 (2016). Copyright 2016 Springer Nature], (b) Wu et al.[87] [reprinted with permission from Wu et al., Nat. Commun. **11**, 521 (2020). Copyright 2020 Springer Nature], and (c) Xu et al.[79] [adapted with permission from Xu et al., Energy Environ. Sci. **13**, 830 (2020). Copyright 2020 The Royal Society of Chemistry]. (d) Performance of various solar vapor generation devices reported in recent literature. The solid symbols represent devices that reuse latent heat to achieve >100% efficiency as defined by Eq. (23). All experiments were performed under one-Sun solar illumination excluding [i], where 900 W/m^2 of electrical heating was used.

desalination systems.[78] Zhang et al. theoretically demonstrated the performance of a closed solar vapor generation system can be significantly enhanced by optimizing the geometrical configuration of the device without any changes to materials.[86] The same group [Xu et al., see Figs. 7(c) and 7(d)] experimentally demonstrated record-high vapor and water production using commercially available and low-cost materials based on the principle of heat and mass transport optimization.[79] Therefore, it is essential to develop device-level, in-depth modeling tools that describe the fundamental heat and mass transport and quantitatively guide design and optimization. On the other hand, further practical opportunities also lie in reducing the material cost and improving the robustness of solar vapor generation devices.[7,78,83] For example, the device is expected to be durable and contaminant-free during a long-term

operation,[76,87] where both the material-level and device-level efforts are required.

C. Electronics cooling devices

In the field of high-performance electronics, the potential for a bottleneck due to heat dissipation limitations is a major concern.[90] For instance, significant enhancement of power switching and radio frequency devices is expected with the implementation of gallium nitride (GaN) and gallium oxide (Ga$_2$O$_3$) microelectronics components.[91] However, thermal management is extremely challenging due to intense, localized heating (~1 kW/cm^2) generated by these devices during operation.[16,91,92] High-flux and efficient cooling strategies are needed to maintain

low enough operating temperatures to sustain good performance and prolong device lifetime.[93,94] Pool boiling is commonly used in power generation and has been explored as a thermal management strategy,[95–98] but the transient nature of boiling causes undesirable temperature fluctuations. Additionally, the evaporator must be larger than the bubble length scale (∼millimeters) to prevent a single bubble from covering the evaporator in an insulating vapor layer, meaning implementation is not practically scalable to microelectronics. Even better performance has been demonstrated with flow boiling in microchannels, but this approach has the drawback of high pumping power requirements and flow instabilities leading to both pressure and temperature fluctuations.[99–101] Thus, pure thin film evaporation (i.e., without boiling) from wicks is a promising electronics cooling strategy not only due to the passive supply of coolant but also owing to its pressure and temperature stability. However, coupling of flow resistance, capillary pressure, and thermal resistance has hindered the performance of monoporous wicks, limiting the efficiency of heat dissipation at high fluxes.[15,32,102–104] State-of-the-art nanofabrication techniques and recent advances in our understanding of evaporation kinetics have led to the demonstration of hierarchical wicks designed to decouple these three characteristics.[62] While this concept already shows promising results, there is much room for further enhancement via optimization of wick geometry, integration of high thermal conductivity materials, and development of fabrication techniques that create more advantageous hierarchy.

The literature contains a rich body of work addressing device-level modeling of capillary-fed, thin film evaporation into pure vapor,[15,32,33,105–108] including for heat pipes and vapor chambers, two commonly used devices for electronics cooling. Since liquid supply is often a limiting factor for these devices, the capillary-driven flow analysis described in Sec. II should be applied to account for the dryout limit in the design process.[16,109,110] The general approach to thermal modeling of these devices is to use Eq. (18) to specify the boundary conditions between coupled wick and vapor domains that are governed by the continuum conservation equations (mass, momentum, energy). By this method, $p_{v,\infty}$ and $T_{v,\infty}$ are taken as the pressure and temperature of vapor in the section of the device adjacent to the evaporator. The resistance in the continuum region between the evaporator and condenser (R_{vapor}) is then dependent on the device geometry, orientation with respect to body forces (e.g., gravity), and fluid properties. R_{wick} depends on the wick structure's geometry, thermophysical properties of the solid and liquid, and flow conditions within the wick. As such, both R_{vapor} and R_{wick} can be tuned through innovation of device architecture and material selection, but the kinetic resistance remains as a fundamental property of the fluid. Therefore, the working fluid and operating conditions are key variables for tuning the heat transfer efficiency of devices operating in the kinetically limited regime. However, as shown in Fig. 3, it is often not possible to choose a fluid and operating conditions that optimize both the capillary and evaporation figures of merit. It is thus desirable to engineer wicking structures that meet heat flux constraints even when a fluid of low M_{cap} is used in order to allow flexibility to improve the heat transfer efficiency of kinetically limited evaporation devices via fluid selection.

Figure 8 shows the simulated cooling performance of a wick in pure vapor conditions. Conduction in the wick is modeled by
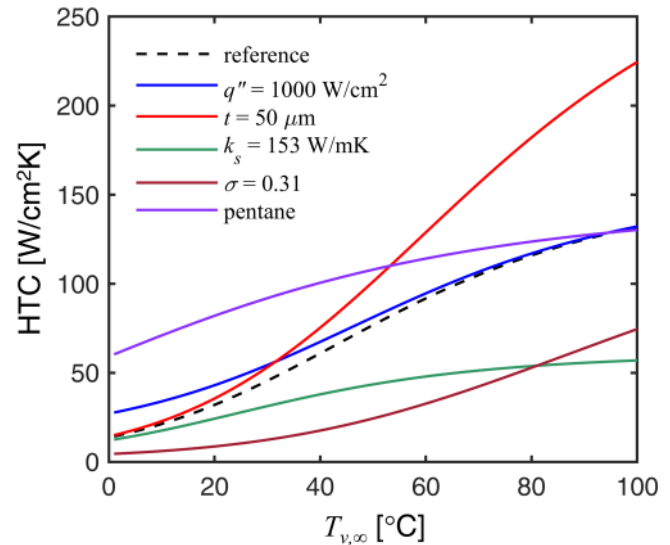

FIG. 8. Simulated evaporative cooling performance for thin film evaporation from a wick into pure vapor; the HTC is defined according to Eq. (5). Heat transfer in the wick and at the liquid–vapor interface are modeled using Eq. (7) and the Schrage equation [Eq. (18)], respectively. The curve labeled as "reference" indicates the simulation results based on parameters $q'' = 100$ W/cm², $t = 100\,\mu m$, $k_s = 398$ W/mK, $\sigma = 1$, and water as the working fluid. Each of the remaining results is labeled by a specific parameter, indicating only the value of the corresponding parameter that changed while all other parameters are the same as the "reference." For example, the curve labeled as "$q'' = 1000$ W/cm²" shows the simulation results based on parameters $q'' = 1000$ W/cm², $t = 100\,\mu m$, $k_s = 398$ W/m K, $\sigma = 1$, and water as the working fluid. k_{wick} is calculated using the Maxwell model [Eq. (10)] where $k_l = 0.60$ W/m K for water and $k_l = 0.11$ W/m K for pentane. Code for this model can be found in the supplementary material.

Eq. (7), where k_{wick} is determined by the Maxwell model [Eq. (10)]. The Schrage equation [Eq. (18)] is used to model heat transfer at the liquid–vapor interface with $p_{v,\infty} = p_{sat}(T_{v,\infty})$ and $\sigma_e = \sigma_c = \sigma$. The reference conditions in Fig. 8 correspond to $q'' = 100$ W/cm² (representative heat dissipation required for electronics cooling[4]), $t = 100\,\mu m$, $k_s = 398$ W/m K (copper at 20 °C[26]), and $\sigma = 1$, with water as the working fluid. The liquid thermal conductivity is set to $k_l = 0.60$ W/m K for water and $k_l = 0.11$ W/m K for pentane, and the porosity of the wick is $\phi = 0.5$. To capture the importance of the temperature dependence of the thermophysical properties of the working fluid, the enthalpy of vaporization and saturation pressures at the interface and far field are extracted from the REFPROP database.[111] The reference curve in Fig. 8 shows that the HTC increases with vapor temperature ($T_{v,\infty}$) for the chosen conditions, reflecting the positive slope of M_{evap} for water in this temperature range (Fig. 3). High-performance electronics are known to generate hot spots where the heat flux can locally exceed 1000 W/cm².[16,91,92] Holding other parameters constant while increasing the heat flux to 1000 W/cm² (see the blue curve in Fig. 8) results in a 93% enhancement of the HTC at $T_{v,\infty} = 1$ °C due to the tendency of $R_{kinetic}$ to decrease with interface temperature at these working conditions. As the far field vapor

temperature increases, the effect of heat flux diminishes since R_{wick} becomes more prominent. On the other hand, reducing the wick thickness to $t = 50\,\mu$m (bright red curve) has little effect at low temperatures (e.g., $T_{v,\infty} < 30\,°$C) due to the dominance of $R_{kinetic}$ but increases the HTC by 70 % at $T_{v,\infty} = 100\,°$C. By the same reasoning, decreasing the solid thermal conductivity to $k_{s-} = 153$ W/mK (silicon at $20\,°$C,[26] green curve) has a small impact at low temperature (e.g., $T_{v,\infty} < 20\,°$C) but increasingly hampers heat transfer as $T_{v,\infty}$ rises. Reducing the accommodation coefficient to

$\sigma = 0.31$ (dark red curve)—better reflecting the experimental measurements in Fig. 4(c)—decreases the HTC by more than 40% across the entire range of $T_{v,\infty}$. This result highlights the importance of accurately determining the accommodation coefficient and mitigating contamination buildup at the liquid–vapor interface. The importance of the choice of working fluid and operating temperature is exemplified by comparing pentane (purple curve) to the dashed reference curve in Fig. 8. A 320% enhancement of the HTC at $T_{v,\infty} = 1\,°$C is achieved by switching to pentane, but
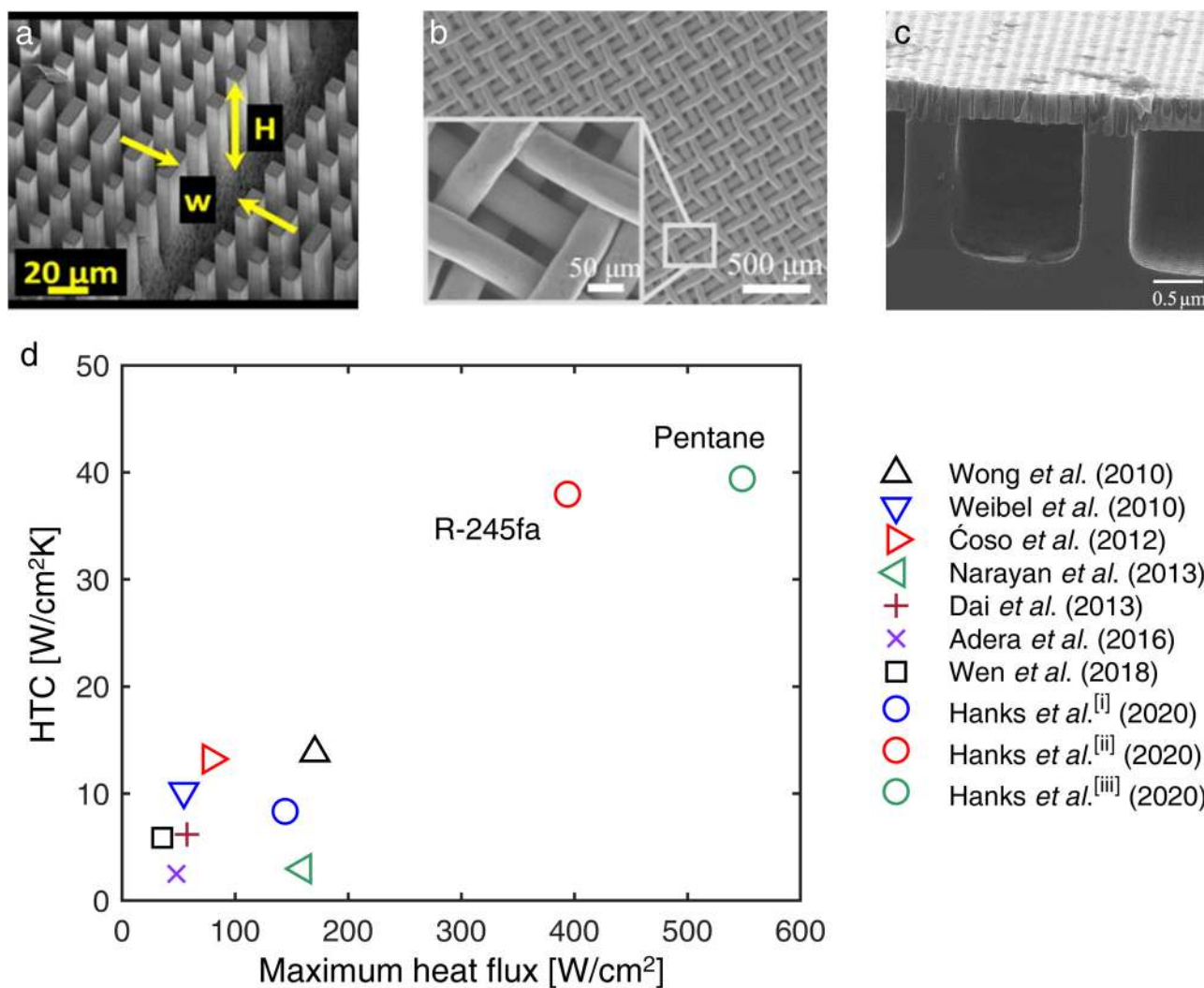

FIG. 9. (a)–(c) Scanning electron micrographs of capillary pumped evaporators reported by (a) Ćoso et al.[14] [adapted with permission from Ćoso et al., J. Heat Transfer **134**, 101501 (2012). Copyright 2012 American Society of Mechanical Engineers], (b) Wen et al.[116] [adapted with permission from Wen et al., Nano Energy **51**, 373 (2018). Copyright 2018 Elsevier], and (c) Hanks et al.[62] [reprinted with permission from Hanks et al., ACS Appl. Mater. Interfaces **12**, 7232 (2020). Copyright 2020 American Chemical Society]. (d) Performance of various capillary-driven evaporators reported in the literature. We used the definition of Eq. (5) for the HTC where T_{wick} was taken as the temperature at the interface between the wick and the substrate. For data points from studies of devices designed for capillary-fed boiling, we chose the data point with the highest heat flux before the onset of nucleate boiling. The working fluid was water unless otherwise noted, Hanks et al. collected data for [i] water, [ii] R-245 fa, and [iii] pentane.

water becomes a more efficient heat transfer fluid at $T_{v,\infty} \approx 96\,°C$ as its M_{evap} approaches that of pentane. Overall, Fig. 8 demonstrates that wick material and geometry, fluid properties, and operating conditions (flux and temperature) significantly impact thermal transport for thin film evaporation into pure vapor.

While HTC is one key metric for electronics cooling, the wick must also be capable of dissipating the target thermal load. In fact, the overall performance of pure thin film evaporation for thermal management is typically limited by the trade-off between achieving high dryout fluxes or efficient heat transfer.[15,103,112] This design limitation is an inherent weakness of monoporous wicks due to unfavorable coupling of viscous resistance to liquid flow, capillary pressure, and thermal resistance. As an example, the widely used Kozeny–Carman equation[113] predicts that the intrinsic permeability of packed media scales with the square of the particle diameter ($K' \sim d_{particle}^2 \sim d_{wick}^2$), whereas the maximum capillary pressure scales with the inverse of the pore diameter ($\Delta p_{max} \sim d_{wick}^{-1}$). Meanwhile, larger pores present a larger thin film resistance as the thermal path from the solid to the interface is lengthened. The consequence is a limited design space where optimizing the wick geometry for dryout heat flux requires penalizing the HTC.[15,103] Since high thermal resistance tends to cause boiling, one popular strategy has been to design wicks with the intention of triggering nucleate boiling within the wicking structure.[112,114–117] In this capillary-fed boiling mode, a thick wick can be utilized since the generation of vapor within the structure somewhat decouples thermal resistance from wick thickness, resulting in a high capillary limit without drastically increased thermal resistance. However, capillary-fed boiling comes with the drawback of spatially varying, transient temperature fluctuations produced by bubble nucleation. Thus, there is still much room for innovation in the pure thin film evaporation regime since a passive, stable, and well-controlled thermal management solution is preferable for electronic device cooling. The key challenge is to overcome the competitive relationship between viscous losses and capillary pressure in order to maximize the dryout heat flux without increasing thermal resistance. Conveniently, enhancement of the maximum capillary pressure and of the HTC can be attained by shrinking pore sizes only in the vicinity of the liquid–vapor interface. This observation has led to the design of tiered, hierarchical wicks;[62,118] structures comprised of a thin layer of smaller pores at the interface to sustain large capillary pressures and facilitate heat transfer supported by a base layer of larger pores designed to reduce viscous losses [Fig. 9(c)]. This biporous structure largely decouples heat transfer and capillary pressure from fluid flow in the wick, giving access to a design regime with greatly enhanced dryout heat flux and HTC.

Figure 9 shows a few examples of capillary-fed evaporators along with data for thin film evaporation performance of various recent studies.[14,32,62,112,119–121] We note that many of the aforementioned studies also explored capillary-fed boiling and reported better performance in that regime; here, we chose the highest heat flux point discernably inside the thin film evaporation regime to represent their data. The slight exceptions to the thin film criteria are as follows: Narayanan *et al.* used an air jet to aid vapor removal, evaporation constituted $\approx 64\%$ of the heat flux at the data point in Fig. 9(d);[119] Dai *et al.* reported boiling at lower heat fluxes but did not observe bubbles in their wick at the data point shown

in Fig. 9(d);[120] Hanks *et al.* pumped liquid to their sample, but liquid supply to the evaporating region was completely passive.[62] We note that the use of a tiered hierarchical structure allowed for the use of low surface tension working fluids (R-245 fa, pentane) at high heat fluxes due to decoupling of viscous losses and capillary pumping capability.[62] These devices were limited by failure due to boiling inside of the fragile structure rather than liquid supply, resulting in the low surface tension fluids outperforming water since their superior M_{evap} provided lower thermal resistance. These tiered, hierarchical wicks show great promise for further design optimization and are particularly advantageous in applications such as electronics cooling where low surface tension dielectric fluids are more desirable than water.

Much opportunity lies in breaking down the barriers to practical implementation of the complicated wick structures being proposed for high-performance electronics cooling. The first barrier is that lab scale demonstrations often involve incompatible, expensive, and/or non-scalable fabrication methods. For example, the tiered, hierarchical wick reported by Hanks *et al.* required multi-step cleanroom fabrication procedures for two wafers.[62] Feasible integration of these innovative wicks into a manufacturable product requires practical and scalable fabrication and materials processing techniques that create multi-scale and multi-layer porous structures. Furthermore, these methods must be compatible with high thermal conductivity materials since thermal performance is extremely sensitive to R_{wick} for evaporation into pure vapor. Recent works have highlighted template self-assembly as a cost-effective, scalable fabrication strategy for high thermal conductivity wicks,[117,122] even demonstrating reasonable conformality over microstructured substrates.[122,123] However, defect control and hierarchy remain challenging for template self-assembly. Other barriers, including longevity and contamination mitigation, similarly present engineering challenges that lie at the intersection of materials processing with heat and mass transfer design.

V. CONCLUSIONS

We have presented a comprehensive review of heat and mass transfer analysis for capillary-fed, thin film evaporation devices that can be used to construct detailed models of application-specific systems. A key modeling distinction is that transport of vapor from the liquid–vapor interface to the far field is greatly dependent on the ambient conditions, that is, whether the ambient is air or pure vapor. In pure vapor, the kinetic resistance of the Knudsen layer is the dominant factor for mass transport, whereas air ambient systems have much lower operating heat fluxes due to diffusive transport resistance. Understanding these governing physics is vital to progress in the field as improving device performance is not only a material's problem, but also a matter of optimizing heat and mass transfer. Although material breakthroughs will be valuable for improving the durability and cost-effectiveness of evaporators for various applications, comprehensive heat and mass transfer modeling tools have the potential to stimulate significant performance enhancement.

The challenges and opportunities in capillary-fed, thin film evaporation are interdisciplinary and multiscale in nature. At the molecular and microscopic scale, our fundamental understanding

of the liquid–vapor interface and the kinetics of phase change remains limited. Namely, our understanding of the mass accommodation coefficient used in the Schrage equation and other kinetic theory-based models is not satisfactory, as evidenced by the discrepancy between MD calculations and experimental measurements. On the experimental side, three key challenges need to be overcome: non-invasive temperature sensing at the liquid–vapor interface, contaminant mitigation, and experimental sensitivity. Developing a better understanding of the mass accommodation coefficient will become increasingly critical to device design as performance approaches the limits imposed by the interface. At the systems level, solar vapor generation is an example of an application where heat and mass transfer optimization offers promising returns, despite much focus in recent literature on novel wick materials. Recent publications have shown that water production and solar vapor efficiency can be greatly enhanced by recovering the latent heat and designing to minimize heat loss, even when using simple materials. However, wick material and architecture development are highly impactful for electronics cooling devices since their operation pushes the limits of capillary liquid supply and the thermal resistance of the wick itself is greatly important. New advances in nanofabrication techniques will be vital for making hierarchical wick architectures that are scalable to chip size, cost-effective, and facilitate high-performance thin film evaporation. There are abundant opportunities for interdisciplinary research efforts to improve evaporative devices and thus positively impact many sectors, such as power generation, water purification, and cooling technologies.

SUPPLEMENTARY MATERIAL

See the supplementary material for the following: Codes for the solar vapor generation device model described in Sec. IV B and the electronics cooling device model described in Sec. IV C have been made available online. The files containing these codes are packaged as "AirAmb_Efficiency" and "PureVapor_HTC," respectively.

ACKNOWLEDGMENTS

DATA AVAILABILITY

The data that support the findings of this study are available from the corresponding author upon reasonable request.

REFERENCES

[1]R. Beebe, J. Qual. Maint. Eng. **9**, 102 (2003).
[2]C. Chen, Y. Kuang, and L. Hu, Joule **3**, 683 (2019).
[3]N. H. Aly and A. K. El-Fiqi, Desalination **158**, 143 (2003).
[4]M. Bulut, S. G. Kandlikar, and N. Sozbir, Heat Transfer Eng. **40**, 1551 (2019).
[5]O. Amer, R. Boukhanouf, and H. G. Ibrahim, Int. J. Environ. Sci. Dev. **6**, 111 (2015).
[6]J. L. Plawsky, A. G. Fedorov, S. V. Garimella, H. B. Ma, S. C. Maroo, L. Chen, and Y. Nam, Nanoscale Microscale Thermophys. Eng. **18**, 251 (2014).
[7]P. Tao, G. Ni, C. Song, W. Shang, J. Wu, J. Zhu, G. Chen, and T. Deng, Nat. Energy **3**, 1031 (2018).
[8]Y. Nagata, K. Usui, and M. Bonn, Phys. Rev. Lett. **115**, 236102 (2015).
[9]J. Julin, M. Shiraiwa, R. E. H. Miles, J. P. Reid, U. Pöschl, and I. Riipinen, J. Phys. Chem. A **117**, 410 (2013).
[10]P. E. Mason, J. Phys. Chem. A **115**, 6054 (2011).
[11]J. Lee, T. Laoui, and R. Karnik, Nat. Nanotechnol. **9**, 317 (2014).
[12]Q. N. Pham, B. Shao, Y. Kim, and Y. Won, ACS Appl. Mater. Interfaces **10**, 16015 (2018).
[13]L. Zhou, Y. Tan, J. Wang, W. Xu, Y. Yuan, W. Cai, S. Zhu, and J. Zhu, Nat. Photonics **10**, 393 (2016).
[14]D. Ćoso, V. Srinivasan, M.-C. Lu, J.-Y. Chang, and A. Majumdar, J. Heat Transfer **134**, 101501 (2012).
[15]G. Vaartstra, Z. Lu, and E. N. Wang, Int. J. Heat Mass Transfer **136**, 170 (2019).
[16]Z. Lu, T. R. Salamon, S. Narayanan, K. R. Bagnall, D. F. Hanks, D. S. Antao, B. Barabadi, J. Sircar, M. E. Simon, and E. N. Wang, IEEE Trans. Compon. Package Manuf. Technol. **6**, 1056 (2016).
[17]G. Ni, G. Li, S. V. Boriskina, H. Li, W. Yang, T. Zhang, and G. Chen, Nat. Energy **1**, 16126 (2016).
[18]H. Ghasemi, G. Ni, A. M. Marconnet, J. Loomis, S. Yerci, N. Miljkovic, and G. Chen, Nat. Commun. **5**, 4449 (2014).
[19]T. Li, H. Liu, X. Zhao, G. Chen, J. Dai, G. Pastel, C. Jia, C. Chen, E. Hitz, D. Siddhartha, R. Yang, and L. Hu, Adv. Funct. Mater. **28**, 1707134 (2018).
[20]X. Wu, L. Wu, J. Tan, G. Y. Chen, G. Owens, and H. Xu, J. Mater. Chem. A **6**, 12267 (2018).
[21]F. Zhao, X. Zhou, Y. Shi, X. Qian, M. Alexander, X. Zhao, S. Mendez, R. Yang, L. Qu, and G. Yu, Nat. Nanotechnol. **13**, 489 (2018).
[22]A. Faghri, J. Heat Transfer **134**, 123001 (2012).
[23]P. G. de Gennes, F. Brochard-Wyart, and D. Quéré, *Capillarity and Wetting Phenomena*, 1st ed. (Springer Science, New York, 2004).
[24]H. C. Brinkman, Appl. Sci. Res. **A1**, 27 (1947).
[25]S. Whitaker, Transp. Porous Media **1**, 3 (1986).
[26]J. H. Lienhard IV and J. H. Lienhard V, *A Heat Transfer Textbook*, 4th ed. (Dover, 2012).
[27]Z. Lu, K. L. Wilke, D. J. Preston, I. Kinefuchi, E. Chang-Davidson, and E. N. Wang, Nano Lett. **17**, 6217 (2017).
[28]R. W. Schrage, "A theoretical study of interphase mass transfer," Ph.D. thesis (Columbia University, 1954).
[29]T. Ytrehus, Multiphase Sci. Technol. **9**, 205 (1997).
[30]R. Ranjan, J. Y. Murthy, and S. V. Garimella, Int. J. Heat Mass Transfer **54**, 169 (2011).
[31]G. P. Peterson and L. S. Fletcher, J. Thermophys. Heat Transfer **1**, 343 (1987).
[32]S. Adera, D. Antao, R. Raj, and E. N. Wang, Int. J. Heat Mass Transfer **101**, 280 (2016).
[33]T. Liu, M. T. Dunham, K. W. Jung, B. Chen, M. Asheghi, and K. E. Goodson, Int. J. Heat Mass Transfer **152**, 119569 (2020).
[34]M. T. Barako, A. Sood, C. Zhang, J. Wang, T. Kodama, M. Asheghi, X. Zheng, P. V. Braun, and K. E. Goodson, Nano Lett. **16**, 2754 (2016).
[35]H. Hu, J. A. Weibel, and S. V. Garimella, Int. J. Heat Mass Transfer **136**, 373 (2019).
[36]L. M. K. Boelter, H. S. Gordon, and J. R. Griffin, Ind. Eng. Chem. **38**, 596 (1946).
[37]M. T. Pauken, Exp. Therm. Fluid Sci. **18**, 334 (1998).
[38]F. Carle, B. Sobac, and D. Brutin, Appl. Phys. Lett. **102**, 061603 (2013).
[39]A. F. Mills, *Heat Transfer*, 2nd ed. (Prentice Hall, Upper Saddle River, NJ, 1998).
[40]R. B. Bird, W. B. Stewart, and E. N. Lightfoot, *Transport Phenomena* (John Wiley & Sons, 2007).
[41]L. Zhang, L. Zhao, and E. N. Wang, Int. Commun. Heat Mass Transfer **110**, 104255 (2019).
[42]Y. Sone, Transp. Theory Stat. Phys. **29**, 227 (2000).
[43]R. Marek and J. Straub, Int. J. Heat Mass Transfer **44**, 39 (2001).

[44]V. P. Carey, *Liquid Vapor Phase Change Phenomena: An Introduction to the Thermophysics of Vaporization and Condensation Processes in Heat Transfer Equipment* (CRC Press, 1992).

[45]J. Barrett and C. Clement, J. Colloid Interface Sci. **150**, 352 (1992).

[46]G. A. Bird, *Molecular Gas Dynamics* (Clarendon Press, Oxford, 1976).

[47]Y. P. Pao, Phys. Fluids **14**, 306 (1971).

[48]D. A. Labuntsov and A. P. Kryukov, Int. J. Heat Mass Transfer **22**, 989 (1979).

[49]P. L. Bhatnagar, E. P. Gross, and M. Krook, Phys. Rev. **94**, 511 (1954).

[50]P. Welander, Ark. Fys. **7**, 507 (1954).

[51]K. Aoki, Y. Sone, and T. Yamada, Phys. Fluids A **2**, 1867 (1990).

[52]Y. Sone, *Molecular Gas Dynamics Theory, Techniques, and Applications* (Birkhauser, Boston, 2007).

[53]A. Frezzotti, Phys. Fluids **23**, 030609 (2011).

[54]R. Meland and T. Ytrehus, Phys. Fluids **15**, 1348 (2003).

[55]P. Jafari, A. Amritkar, and H. Ghasemi, J. Phys. Chem. C **124**, 1554 (2020).

[56]A. Frezzotti, Eur. J. Mech. B Fluids **26**, 93 (2007).

[57]Z. Lu, I. Kinefuchi, K. L. Wilke, G. Vaartstra, and E. N. Wang, Nat. Commun. **10**, 2368 (2019).

[58]Z. Liang, T. Biben, and P. Keblinski, Int. J. Heat Mass Transfer **114**, 105 (2017).

[59]Z. Liang, A. Chandra, E. Bird, and P. Keblinski, Int. J. Heat Mass Transfer **149**, 119152 (2020).

[60]J. Gonzalez, J. Ortega, and Z. Liang, Int. J. Heat Mass Transfer **126**, 1183 (2018).

[61]E. Bird, J. Gutierrez Plascencia, and Z. Liang, J. Chem. Phys. **152**, 184701 (2020).

[62]D. F. Hanks, Z. Lu, J. Sircar, I. Kinefuchi, K. R. Bagnall, T. R. Salamon, D. S. Antao, B. Barabadi, and E. N. Wang, ACS Appl. Mater. Interfaces **12**, 7232 (2020).

[63]G. Nagayama and T. Tsuruta, J. Chem. Phys. **118**, 1392 (2003).

[64]R. Meland, Phys. Fluids **15**, 3244 (2003).

[65]R. Meland and T. Ytrehus, Phys. Fluids **16**, 836 (2004).

[66]P. Varilly and D. Chandler, J. Phys. Chem. B **117**, 1419 (2013).

[67]T. Tsuruta, H. Tanaka, and T. Masuoka, Int. J. Heat Mass Transfer **42**, 4107 (1999).

[68]S. Glasstone, K. J. Laidler, and H. Eyring, *The Theory of Rate Processes* (McGraw-Hill Book Company, New York, 1941).

[69]C. A. Ward and G. Fang, Phys. Rev. E **59**, 429 (1999).

[70]D. Bedeaux, S. Kjelstrup, and J. M. Rubi, J. Chem. Phys. **119**, 9163 (2003).

[71]A. Tamir and D. Hasson, Chem. Eng. J. **2**, 200 (1971).

[72]J. D. Smith, C. D. Cappa, W. S. Drisdell, R. C. Cohen, and R. J. Saykally, J. Am. Chem. Soc. **128**, 12892 (2006).

[73]A. H. Persad and C. A. Ward, Chem. Rev. **116**, 7727 (2016).

[74]Y. Li, H. Chen, S. Xiao, M. A. Alibakhshi, C.-W. Lo, M.-C. Lu, and C. Duan, ACS Nano **13**, 3363 (2019).

[75]L. Zhang, Y. Zhu, Z. Lu, L. Zhao, K. R. Bagnall, S. R. Rao, and E. N. Wang, Appl. Phys. Lett. **113**, 163701 (2018).

[76]G. Ni, S. H. Zandavi, S. M. Javid, S. V. Boriskina, T. A. Cooper, and G. Chen, Energy Environ. Sci. **11**, 1510 (2018).

[77]S. He, C. Chen, Y. Kuang, R. Mi, Y. Liu, Y. Pei, W. Kong, W. Gan, H. Xie, E. Hitz, C. Jia, X. Chen, A. Gong, J. Liao, J. Li, Z. J. Ren, B. Yang, S. Das, and L. Hu, Energy Environ. Sci. **12**, 1558 (2019).

[78]Z. Wang, T. Horseman, A. P. Straub, N. Y. Yip, D. Li, M. Elimelech, and S. Lin, Sci. Adv. **5**, eaax0763 (2019).

[79]Z. Xu, L. Zhang, L. Zhao, B. Li, B. Bhatia, C. Wang, K. L. Wilke, Y. Song, O. Labban, J. H. Lienhard, R. Wang, and E. N. Wang, Energy Environ. Sci. **13**, 830 (2020).

[80]J. Li, M. Du, G. Lv, L. Zhou, X. Li, L. Bertoluzzi, C. Liu, S. Zhu, and J. Zhu, Adv. Mater. **30**, 1805159 (2018).

[81]A. K. Menon, I. Haechler, S. Kaur, S. Lubner, and R. S. Prasher, Nat. Sustain. **3**, 144 (2020).

[82]E. Chiavazzo, M. Morciano, F. Viglino, M. Fasano, and P. Asinari, Nat. Sustain. **1**, 763 (2018).

[83]W. Wang, Y. Shi, C. Zhang, S. Hong, L. Shi, J. Chang, R. Li, Y. Jin, C. Ong, S. Zhuo, and P. Wang, Nat. Commun. **10**, 3012 (2019).

[84]J. Li, X. Wang, Z. Lin, N. Xu, X. Li, J. Liang, W. Zhao, R. Lin, B. Zhu, G. Liu, L. Zhou, S. Zhu, and J. Zhu, Joule **4**, 1 (2020).

[85]X. Li, J. Li, J. Lu, N. Xu, C. Chen, X. Min, B. Zhu, H. Li, L. Zhou, S. Zhu, T. Zhang, and J. Zhu, Joule **2**, 1331 (2018).

[86]L. Zhang, Z. Xu, B. Bhatia, B. Li, L. Zhao, and E. N. Wang, Appl. Energy **266**, 114864 (2020).

[87]L. Wu, Z. Dong, Z. Cai, T. Ganapathy, N. X. Fang, C. Li, C. Yu, Y. Zhang, and Y. Song, Nat. Commun. **11**, 521 (2020).

[88]X. Hu, W. Xu, L. Zhou, Y. Tan, Y. Wang, S. Zhu, and J. Zhu, Adv. Mater. **29**, 1604031 (2017).

[89]Y. Kuang, C. Chen, S. He, E. M. Hitz, Y. Wang, W. Gan, R. Mi, and L. Hu, Adv. Mater. **31**, 1900498 (2019).

[90]A.-C. Iradukunda, D. R. Huitink, and F. Luo, IEEE J. Emerging Sel. Top. Power Electron. **8**, 256 (2020).

[91]M. Higashiwaki and G. H. Jessen, Appl. Phys. Lett. **112**, 060401 (2018).

[92]K. R. Bagnall, "Device-level thermal analysis of GaN-based electronics," M.S. thesis (Massachusetts Institute of Technology, 2013).

[93]M. Rosker, C. Bozada, H. Dietrich, A. Hung, D. Via, S. Binari, E. Vivierios, E. Cohen, and J. Hodiak, in *CS MANTECH Conference*, Tampa, FL (2009).

[94]K. R. Bagnall, E. A. Moore, S. C. Badescu, L. Zhang, E. N. Wang, and E. N. Wang, Rev. Sci. Instrum. **88**, 113111 (2017).

[95]S. Fan and F. Duan, Int. J. Heat Mass Transfer **150**, 119324 (2020).

[96]M. S. El-Genk and A. F. Ali, J. Heat Transfer **137**, 041501 (2015).

[97]A. Jaikumar and S. G. Kandlikar, Appl. Therm. Eng. **91**, 426 (2015).

[98]T. M. Anderson and I. Mudawar, J. Heat Transfer **111**, 752 (1989).

[99]G. Liang and I. Mudawar, Int. J. Heat Mass Transfer **146**, 118864 (2020).

[100]E. Sourtiji and Y. Peles, Int. J. Heat Mass Transfer **147**, 119023 (2020).

[101]Y. Zhu, D. S. Antao, D. W. Bian, S. R. Rao, J. D. Sircar, T. Zhang, and E. N. Wang, Appl. Phys. Lett. **110**, 033501 (2017).

[102]D. A. Pruzan, L. K. Klingensmith, K. E. Torrance, and C. T. Avedisian, Int. J. Heat Mass Transfer **34**, 1417 (1991).

[103]Y. X. Wang and G. P. Peterson, J. Thermophys. Heat Transfer **17**, 145 (2003).

[104]Y. Zhu, D. S. Antao, Z. Lu, S. Somasundaram, T. Zhang, and E. N. Wang, Langmuir **32**, 1920 (2016).

[105]G. Patankar, J. A. Weibel, and S. V. Garimella, Int. J. Heat Mass Transfer **119**, 867 (2018).

[106]G. Patankar, J. A. Weibel, and S. V. Garimella, Int. J. Heat Mass Transfer **101**, 927 (2016).

[107]Y. Yadavalli, J. A. Weibel, and S. V. Garimella, IEEE Trans. Compon. Package Manuf. Technol. **5**, 1618 (2015).

[108]C.-K. Huang, C.-Y. Su, and K.-Y. Lee, Exp. Heat Transfer **25**, 1 (2012).

[109]R. Wang, K. Jakhar, and D. S. Antao, Langmuir **35**, 12927 (2019).

[110]K. Baraya, J. A. Weibel, and S. V. Garimella, Int. J. Heat Mass Transfer **136**, 842 (2019).

[111]E. W. Lemmon, I. H. Bell, M. L. Huber, and M. O. McLinden, "Reference Fluid Thermodynamic and Transport Properties Database (REFPROP), Version 9.1," in *NIST Standard Reference Database 23: Reference Fluid Thermodynamic and Transport Properties* (NIST, Gaithersburg, 2018).

[112]J. A. Weibel, S. V. Garimella, and M. T. North, Int. J. Heat Mass Transfer **53**, 4204 (2010).

[113]P. C. Carman, Chem. Eng. Res. Des. **75**, S32 (1997).

[114]S. Sudhakar, J. A. Weibel, F. Zhou, E. M. Dede, and S. V. Garimella, Int. J. Heat Mass Transfer **148**, 119063 (2020).

[115]S. Sudhakar, J. A. Weibel, F. Zhou, E. M. Dede, and S. V. Garimella, Int. J. Heat Mass Transfer **135**, 1346 (2019).

[116]R. Wen, S. Xu, Y. C. Lee, and R. Yang, Nano Energy **51**, 373 (2018).

[117]C. Zhang, J. W. Palko, M. T. Barako, M. Asheghi, J. G. Santiago, and K. E. Goodson, Adv. Funct. Mater. **28**, 1803689 (2018).

[118]D. F. Hanks, Z. Lu, J. Sircar, T. R. Salamon, D. S. Antao, K. R. Bagnall, B. Barabadi, and E. N. Wang, Microsyst. Nanoeng. **4**, 1 (2018).

[119]S. Narayanan, A. G. Fedorov, and Y. K. Joshi, Int. J. Heat Mass Transfer **58**, 300 (2013).

[120]X. Dai, F. Yang, R. Yang, Y. C. Lee, and C. Li, Int. J. Heat Mass Transfer **64**, 1101 (2013).

[121]S.-C. Wong, J.-H. Liou, and C.-W. Chang, Int. J. Heat Mass Transfer **53**, 3792 (2010).

[122]J. W. Palko, H. Lee, C. Zhang, T. J. Dusseault, T. Maitra, Y. Won, D. D. Agonafer, J. Moss, F. Houshmand, G. Rong, J. D. Wilbur, D. Rockosi, I. Mykyta, D. Resler, D. Altman, M. Asheghi, J. G. Santiago, and K. E. Goodson, Adv. Funct. Mater. **27**, 1703265 (2017).

[123]B. Hatton, L. Mishchenko, S. Davis, K. H. Sandhage, and J. Aizenberg, Proc. Natl. Acad. Sci. U.S.A. **107**, 10354 (2010).